Meteoritics & Planetary Science 39, Nr 11, 1869–1887 (2004)
Abstract available online at http://meteoritics.org

Dynamic pyrometamorphism during atmospheric entry of large (~10 micron) pyrrhotite fragments from cluster IDPs

Frans J. M. RIETMEIJER

Department of Earth and Planetary Sciences, University of New Mexico, Albuquerque, New Mexico 87131, USA
E-mail: fransjmr@unm.edu

(Received 19 December 2003; revision accepted 8 May 2004)

Abstract–Petrological changes in Ni-free and low-Ni pyrrhotite, and much less in pentlandite, during atmospheric entry flash-heating of the sulfide IDPs L2005E40, L2005C39, and L2006A28 support 1) ferrous sulfide oxidation with vacancy formation and Fe^{3+} ordering; and 2) Fe-oxide formation and sulfur vapor loss through abundant vesicles. Melting of metastable chondritic aggregate materials at the IDP surface has occurred. All changes, e.g., formation of a continuous maghémite rim, proceeded as solid-state reactions at a peak heating temperature of ~700 °C. This temperature in combination with particle size and density suggest a ~10 km/s^{-1} entry velocity. The IDPs probably belonged to cluster IDPs that entered the atmosphere with near-Earth or Earth-crossing asteroid velocities. They could be debris from extinct or dormant comet nuclei, which is consistent with shock comminution of pyrrhotite in these IDPs.

INTRODUCTION

Interplanetary dust particles (IDPs) collected in the Earth's stratosphere between 17 and 19 km altitude are mostly the solid debris from periodic comets and asteroids, such as P- and D-infrared class objects in the outer asteroid belt that are not well represented by collectable meteorites, and from near-Earth and Earth-crossing asteroids. It is possible that the Earth's gravitational focusing effect delivers collected IDPs mostly from the Koronis and Themis asteroid families (Dermott et al. 1996) although particle size is critical in this argument. The maximum peak-heating temperature of an IDP during atmospheric entry is a function of particle size, density, and atmospheric entry angle and entry velocity. This relationship was promoted as a means to separate low-velocity (<14 km/s) asteroidal from high-velocity (>18 km/s) cometary IDPs (Brownlee et al. 1995). Unambiguous source-classification of individual IDPs can be difficult because very similar particle properties (e.g., morphology, mineralogy, hydration) occur across these velocity groups (Joswiak et al. 2000). Some caution might be advisable as illustrated by the orbital velocity of meteors from the MORP (Halliday et al. 1996) and Prairie Network (Ceplecha et al. 1996) databases showing that the velocities of meteors linked to asteroids range from ~5 to ~24 km/s and low-velocity cometary meteor velocities range from ~6 to ~24 km/s (see Rietmeijer 2000). For example, Geminid meteors with a velocity of 36 km/s are probably fluffy aggregates associated with small asteroids, e.g., 3200 Phaeton. This velocity is even higher than the ~30.5 km/s average velocity of meteors associated with P/comet Encke.

Particle texture and mineral constituents might still be the best indicator for the origin of chondritic IDPs that are either aggregate or non-aggregates particles; the latter resembling CI, CR, and CM meteorite matrix (Rietmeijer 1998, 2002a) (Fig. 1). Reviewing the petrology, mineralogy, and textures of chondritic aggregate IDPs, Mackinnon and Rietmeijer (1987) concluded they are uniquely different from any other materials found among the collected meteorites. Subsequent research supported this conclusion with new data on aggregate IDPs, e.g., principal components (PCs) (Rietmeijer 2002a) and GEMS (Bradley 1994; Bradley et al. 1999), and on stable isotope chemistry (Keller et al. 2000; Messenger 2000; Messenger et al. 2003). Aggregate IDPs clearly represent small solar system bodies other then meteorite parent bodies.

The first major subdivision of all collected IDPs is based on bulk composition: 1) chondritic IDPs; and 2) non-chondritic IDPs (Fig. 1), and raises the question of how particles of these two groups could have become interlinked in the solar nebula, and which is addressed by the hypothesis of hierarchical dust accretion (Rietmeijer 1998). Porous matrix aggregates (~5 micron in size) of PCs (90 nm up to 1000 nm) and 100–500 nm-sized sulfide grains could have formed during early dust accretion into entities we now find

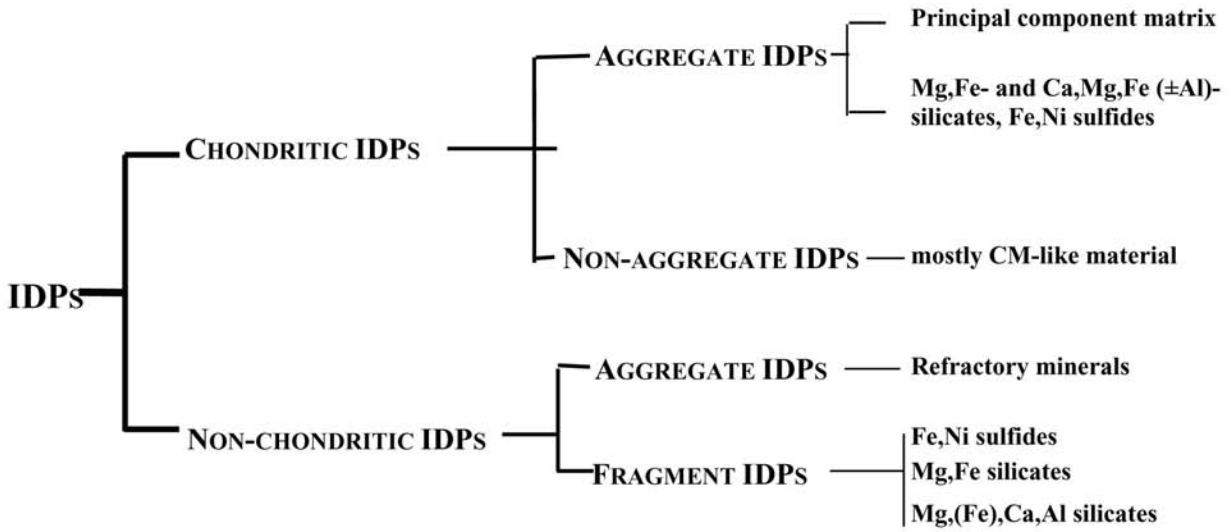

Fig. 1. Chemical and morphological classification of interplanetary dust particles collected in the Earth's lower stratosphere (columns 2 and 3) and mineralogical identification of aggregates and fragments (column 4). Reproduced from Rietmeijer (2002a).

as aggregate IDPs (Rietmeijer 1998). Iron, Ni-sulfides in this size range are present as rounded grains, masses of rounded grains, euhedral pseudohexagonal plates, and equant grains (Klöck and Stadermann 1994; Zolensky and Thomas 1995; Dai and Bradley 2001). They include pyrrhotite (0.1–0.5 wt% Ni), stoichiometric troilite (Ni <5 at%) (minor phase) and pentlandite (up to 30 wt% Ni) (Germani et al. 1990; Thomas et al. 1991; Tomeoka and Buseck 1984; Zolensky and Thomas 1995) and hexagonal pyrrhotite ($0 \le Ni \le 20$ at%), an S-deficient cubic sulfide with ~6 at% Ni and pentlandite (Dai and Bradley 2001). There is also ample observational evidence that larger non-chondritic dust co-accreted with matrix aggregates into 10–15 μm-sized aggregate IDPs (Rietmeijer 1998, 2002a). The non-chondritic dust includes 1) rare refractory Ca, Al-rich IDPs (Zolensky 1987) with extraterrestrial O isotope composition (McKeegan 1987); 2) coarse-grained mostly monomineralic Fe, Ni-sulfide IDPs; and 3) coarse-grained Mg, Fe (±Ca)-silicate IDPs with small amounts of sulfides. These coarse-grained IDPs (Schramm et al. 1989) show two Gaussian size distributions with means at 8.2 μm and 15.6 μm (Rietmeijer 1998). Based on size alone, the first population could be similar to the sulfide and silicate grains in aggregate IDPs, although in IDPs the sulfide grains are generally ~2 to 5 μm in size and include pyrrhotite, a spinel-type sulfide (~1–18 at% Ni), and pentlandite (Rietmeijer 1998; Dai and Bradley 2001).

The second population (mean = 15.6 μm) includes coarse-grained olivine/Fe, Ni-sulfide IDPs (Christoffersen and Buseck 1986; Rietmeijer 1996a), silicate IDPs encrusted by Fe-sulfides and chondritic materials (Steele 1990), and large (mostly) pyrrhotite grains attached to chondritic IDPs (Zolensky and Thomas 1995; Rost et al. 1999). These pyrrhotite IDPs have an average S content of 38.7 wt% and an average Ni content of 1.8 wt% (Schramm and Brownlee 1990). Brownlee et al. (1977) noted that 10–25 μm-sized sulfide and silicate grains occurred in chondritic aggregates, so-called cluster IDPs (Thomas et al. 1995) that broke apart during collection. Co-accretion of these grains and aggregate IDPs are the next step in the hierarchical accretion of solar nebula dust whereby a small number of dust types gradually increase in size and chemical complexity by recycling through evolving protoplanets (Rietmeijer 2002a). Cluster IDPs are the largest step in this hierarchy that is accessible to laboratory study.

Aerobreaking in the Earth's atmosphere to settling velocity (cm s^{-1}) between 100–80 km altitude causes flash-heating wherein the kinetic energy is transformed to heat with resulting thermal equilibration between the IDP surface and interior (Love and Brownlee 1991). Dynamic pyrometamorphic temperatures in unmelted IDPs range from 200–300 °C (Nier and Schlutter 1993) up to ~1150 °C with heating and quench rates on the order of 10^5–10^6 degrees h^{-1} (Rietmeijer 1996a, b, 1998). The interior peak temperature would be lower when a thermal gradient developed due to phase transformations of IDP constituents (Flynn 1995).

I report on features that formed during dynamic pyrometamorphism of three sulfide IDPs. They could have entered the atmosphere as part of a cluster IDP and due to the overall low aggregate density survived with minimal thermal alteration. Each one might have entered the atmosphere individually after liberation from a parent body, on-orbit disruption of aggregates in comet dust trails or in the zodiacal cloud. If so, the high sulfide density resulted in higher peak-heating temperatures than when "shielded" in a decelerating cluster IDP, assuming all other relevant parameters being equal. Aggregate break-up during deceleration in the lower, denser Earth atmosphere would have produced molten sulfide spheres.

EXPERIMENTAL

The IDPs L2005E40, L2005C39, and L2006A28 were collected on large-area, inertial-impact, flat-plate collectors mounted underneath the wings of a NASA ER-2 aircraft flying over west-central North America, October 3–13, 1989. Mackinnon et al. (1982), Warren and Zolensky (1994), and Rietmeijer (1998) reviewed collection and curation procedures. The allocated IDPs were embedded in an epoxy (Spurrs) at the NASA-JSC Curatorial Facility for serial sectioning using a Reichert-Jung Ultramicrotome E used a diamond knife moving at a speed between 0.5 and 0.8 mm s^{-1}. All sulfides in these IDPs showed brittle behavior even when considerable care was taken during ultra-thin section preparation to avoid particle damage. The resulting sections are not universally electron-transparent while thinner sections tended to fall apart. The 80–100 nm thin sections were placed on a holey carbon thin-film supported by a standard 200 mesh Cu grid and housed in a Gatan low-background, double-tilt specimen holder. At least 10 individual, carbon-coated sections of each sample were analyzed using a JEOL 2000FX analytical transmission electron microscope (TEM) operating at an accelerating voltage of 200 keV and equipped with a Tracor-Northern TN-5500 energy dispersive spectrometer (EDS) for in situ analysis of elements with atomic number >11. The probe was 15 nm in diameter. Real-time data acquisition of 150 sec yielded EDS spectra for quantitative analyses using the Cliff-Lorimer (1975) thin-film correction procedure using k-factors that were obtained on natural standards (Mackinnon and Kaser 1987). The location of each crystallographic and chemical analysis was recorded on TEM maps to assess spurious contamination. The particle c-dimension (thickness) perpendicular to the ab-plane in ultra-thin sections was reconstructed from serial sections of known relative positions in the sectioning sequence. Crystallographic data were obtained from selected area electron diffraction (SAED) patterns that were calibrated using an Au-coated holey carbon film analyzed under similar conditions as the samples. Interplanar values for single-crystal patterns have an error of <5% relative; a 10% relative error for polycrystalline ("ring") patterns. Grains were measured on calibrated TEM micrographs with a relative error of <10% expressed as the root-mean-square size, i.e., rms = $(a^2 + b^2)^{1/2}$, where *a* and *b* are two orthogonal dimensions across a grain. Grain sizes and sulfide compositions show Gaussian distributions at 95% significance level based on the ratio of range to standard deviation (1σ) as a function of population size N.

OBSERVATIONS

L2005E40

The pear-shaped particle (9.5 × 6.25 × 6 μm) is an irregular intergrowth of a large pyrrhotite grain and a smaller pentlandite grain (Fig. 2). The IDP diameter, D = [(a + b + c)/3] is 7.3 μm. A 50–125 nm-wide hematite (α-Fe_2O_3) (Table 1) rim is closely

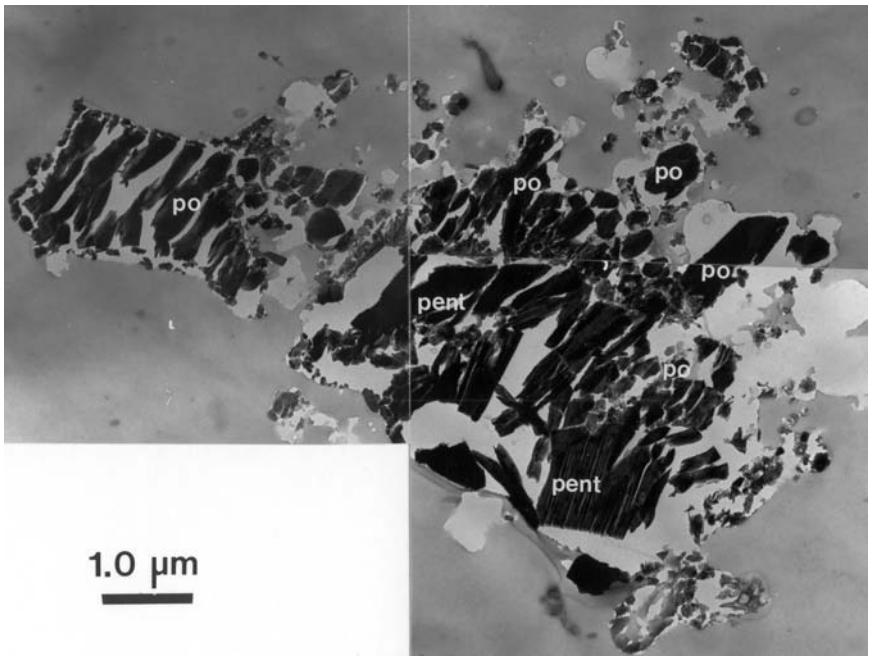

Fig. 2. Transmission electron microscope (TEM) image showing a microtomed thin section of IDP L2005E40 showing pentlandite (pent) surrounded by pyrrhotite (po). The shattered nature of the IDP is obvious and resulted in significant sample loss (white area shows the particle outline). A narrow Fe-oxide rim is visible on pyrrhotite on right-hand side. A silicate patch shows as a light-gray lobe in the lower right-hand. The embedding epoxy shows as the dark gray background.

Table 1. Comparison of interplanar spacing values (nm) of Fe-rich grains in rims on three coarse-grained IDPs based on SAED analysis compared to Fe-oxides from the J.C.P.D.S. files: 24-81 (cubic maghémite), 25-1402 (tetragonal maghémite), 24-72 (hexagonal hematite), and 19-629 (magnetite).

L2005E40	L2006A28	L2005C39	Cubic maghémite	Tetragonal maghémite	Hexagonal hematite	Magnetite
				2.50		
1.40					1.40	
	0.83		0.835	0.83		0.84
				0.79		
	0.62			0.69		
	0.59	0.59	0.59	0.59		
	0.57					
		0.54		0.53		
		0.50				
0.48	0.48	0.48	0.48	0.48		0.485
	0.42	0.45	0.42	0.43		
	0.36	0.38	0.37	0.37	0.37	
		0.33	0.34	0.34		
	0.31			0.32		
	0.30	0.30	0.295	0.295		0.30
			0.28	0.28		
	0.26	0.26	0.26	0.26	0.27	
			0.25	0.25	0.25	0.25
0.24			0.24	0.24		0.24

Table 2. Mean sulfide compositions (atomic ratios) ± one sigma standard deviation in sulfide IDPs L2005E40 and an intergrowth of two major sulfides, L2006A28 and L2005C39.

	Fe	Ni	S
L2005E40			
Major sulfide (1)	44.4 ± 2.3	3.3 ± 0.9	52.3 ± 1.8
Small grains	43.3 ± 2.0	5.7 ± 1.0	51.0 ± 1.6
Laths	41.0 ± 6.1	8.2 ± 3.4	50.8 ± 3.7
Major sulfide (2)	32.0 ± 2.6	18.3 ± 0.45	49.7 ± 2.6
Ultrafine-grained zone on (2)	34.5 ± 3.9	15.5 ± 4.1	50.0 ± 2.9
L2006A28			
Bulk IDP sulfide	44.8 ± 2.3	1.2 ± 0.6	54.0 ± 2.5
L2005C39			
Bulk IDP sulfide	49.5 ± 0.9	Trace	50.4 ± 1.6

associated with pyrrhotite; less so with pentlandite. Isolated Fe-oxide grains up to ~20 nm in size form a partial rim on small, randomly distributed, ferromagnesiosilica patches that occur at the particle surface. Fe-oxide nanocrystals (8.0 nm; 1σ = 2.8 nm) are scattered in these patches.

The average composition indicates low-Ni (1.2–4.5 at%) pyrrhotite, $Fe_{0.85}Ni_{0.06}S$ (Table 2), with a range from $Fe_{1.03}Ni_{0.09}S$ to $Fe_{0.63}Ni_{0.07}S$ (Fig. 3a). This range and average sulfur content are similar to those of large low-Ni pyrrhotite grains in other IDPs (Table 3). Dark-field imaging of pyrrhotite shows a zone with a distinct mottled texture. It is much thicker when present at the particle surface than along the margins of the shattered grains (Fig. 4). The interiors without the mottled texture in this and the other IDPs are single-crystal, low-Ni pyrrhotite (Table 4). The high-Ni sulfide single-crystal (Table 4) has a unit cell that resembles pyrrhotite. Previously Alexander et al. (1989) found that Ni-rich sulfide in the matrix of unequilibrated ordinary chondrites had pyrrhotite-like d-values. The pentlandite unit cell heated to 250–300 °C resembles pyrrhotite (Likhachev and Brauer 1969). Pentlandite identification in this IDP relies on chemical composition (Fig. 3a), and is similar to pentlandite identified in another IDP (Table 5).

All pentlandite and pyrrhotite single-crystal parts display a weak lineation due to small crystallographically controlled maghémite lamellae. This oxide identification, as well as in the other IDPs, is based an SAED data. The interior parts of pentlandite grains typically consist of narrow, structurally discontinuous, lamellae oriented parallel to the c-axis. Disseminated Fe-oxide grains cause a mottled texture of these lamellae. Other pentlandite grains have a regular stratification of narrow mottled bands separated by an equally narrow lamella of amorphous material with embedded ultrafine maghémite grains (Fig. 5).

Sulfide-ferromagnesiosilica interactions produced a distinct layered sequence (Fig. 6). First, there is a 55 to 75-nm wide zone defined by abundant mostly rounded to irregular, ultrafine grains that occurs on top of the underlying sulfide. When present on pentlandite, this zone consists of pentlandite grains (Table 2). This granular zone on pyrrhotite, however, is a ferromagnesiosilica material with high but variable S, Ni and Al content (Table 6, #1). There is a marked transition to the next zone of variable thickness wherein lath-shaped, rounded and angular sulfide grains float in ferromagnesiosilica patches. The sulfur content decreases

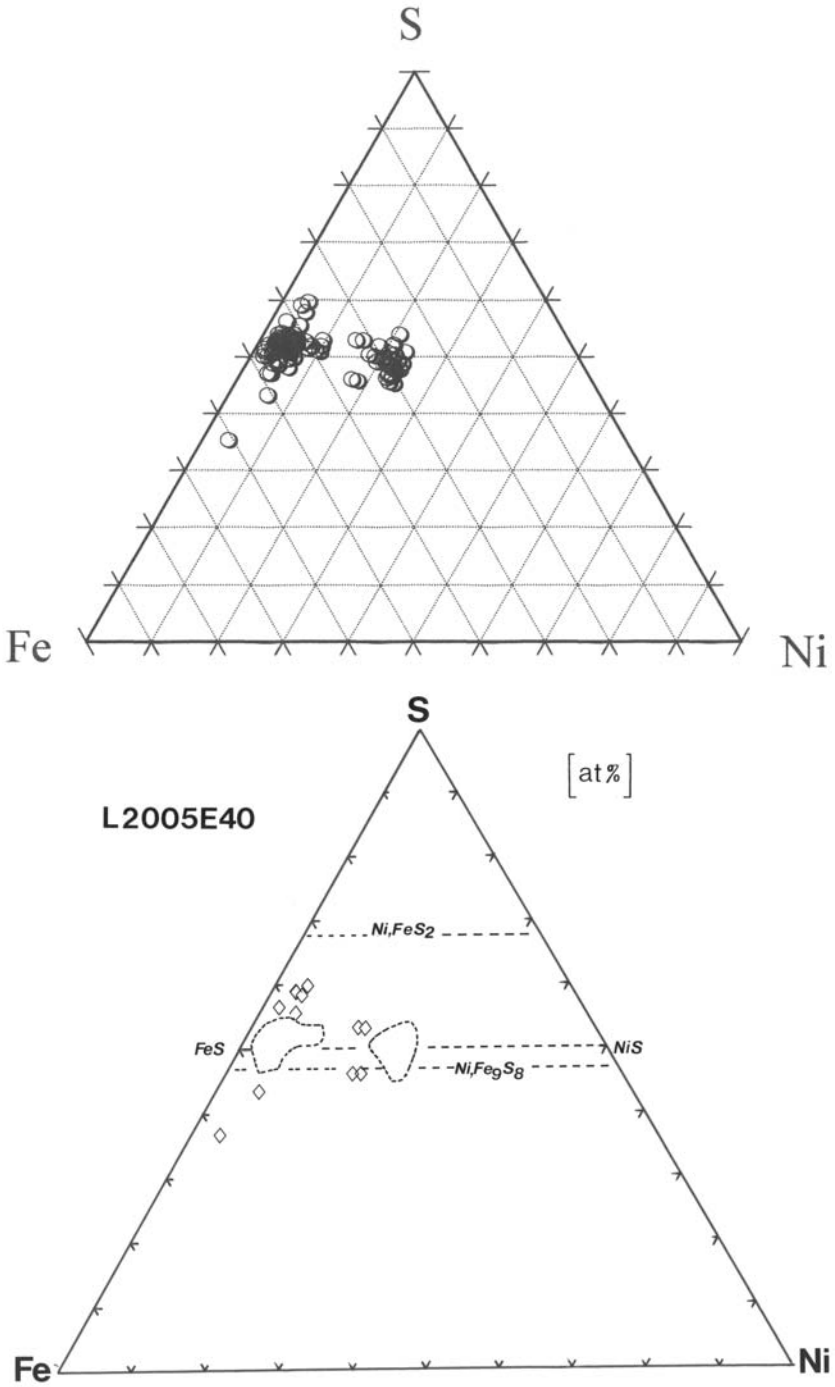

Fig. 3. Sulfide compositions in IDP L2005E40 in the ternary Fe-Ni-S (at%) system: a) the lowest-sulfur data point was adjacent to the Fe-oxide rim; b) the dashed field boundaries indicate the average compositions of low-Ni pyrrhotite and pentlandite (cf. Table 2) and their extensions across the compositional gap. Diamonds represent the outlier compositions discussed in the text. The horizontal dashed lines mark the (Fe, Ni)/S ratios of pentlandite, troilite, and pyrite.

with increasing distance from the underlying sulfide. The amorphous matrix of the patches has variable amounts of embedded ultrafine (4–10 nm; up to 30 nm) olivine, pyroxene, and sulfide grains. The mottled, rounded and angular, high-Ni pyrrhotite (Table 2) grains are mostly 100–375 nm in size, but can be as small as 40 nm. There is no clear cut-off at either end of their size range. Mottled high-Ni pyrrhotite (Table 2) laths with an average aspect ratio 0.22 (range = 0.1–0.35) are oriented perpendicular or almost perpendicular to the zone boundary (Fig. 6). Rosettes of laths are present. The mottled texture of these embedded grains and laths resembles that of the underlying sulfide. These mottled

Table 3. Range and mean sulfur content (at%) of low-Ni and Ni-free pyrrhotite in IDPs L2005E40, L2006A28, and L2005C39 compared with [1] low-Ni (<5 at%) pyrrhotite from 30 IDPs (Zolensky and Thomas 1995) and [2] low-Ni (0.4–3.5 at%) pyrrhotite in a "low-Ca" hydrated IDP (Tomeoka and Buseck 1984). The author recalculated the data from both papers; N: number of data.

IDP	Range	Mean	1	N
L2005E40	47.2–56.2	52.3	1.8	52
L2006A28	49.4–60.9	54.0	2.5	35
L2005C39	48.6–52.2	50.5	0.9	59
[1]	48–57	53	–	168
[2]	50.4–53.5	51.9	1.1	8

grain compositions form the bulge on the pyrrhotite field towards the pentlandite field (Fig. 3b). The compositions of the ultrafine-grained sulfide zone cause the main pentlandite field to expand towards lower Ni contents including some extreme compositions, viz. $Fe_{0.64}Ni_{0.36}S$ (Fig. 3b). This zone can be capped by a thin layer of S- and Ni-free silicates (Table 6, #2 and #3) followed by a discontinuous Fe-oxide rim or it can be directly overlain by Fe-oxide crystals (~50 nm) commonly forming a rim. The silicate zone is often poorly developed or even absent.

The formation of a Fe-oxide rim on pyrrhotite produced a very distinctly layered sequence within pyrrhotite consistent with a thermal gradient perpendicular to the particle surface (Fig. 7), viz.

Z1

A 55–70 nm wide zone with a mottled texture. It contains randomly distributed Fe-rich plates (up to ~10 nm thick) with 1.3 nm lattice fringes consistent with *hkl* (002) maghémite or *hkl* (001) hematite. The SAED data indicate pyrrhotite (3C), pyrrhotite (4C) or both (Table 4). They have an increasingly smaller size towards the grain exterior along with increasing amounts of random Fe-oxide nanocrystals. The transition from single-crystal pyrrhotite to this mélange of fine-grained pyrrhotite and Fe-oxides occurs gradually towards the grain boundary or particle surface. Fe-oxide plates are a few unit-cell layers thick and oriented parallel to the host (100) plane. Scattered domains with a high density of Fe-oxide plates are common. The overall density of such domains increases from the interior of the grain to its margin. This feature is similar to the mottled texture along the grain boundary of fractured sulfide sub-grain (cf. Fig. 4) but wherein its development is much less intense than in domains at the Z1/Z2 interface. Here they form a well-defined zone parallel to this interface.

Z2

A 140–180 nm wide zone with the same Z1 mottled texture is uniquely characterized by crystallographically aligned vesicles that, close to the Z1/Z2 interface, are typically small and round but limited in number (Fig. 7). They sharply increase in number and size towards the iron-oxide rim. Large vesicles (5–10 nm; up to ~50 nm) have a euhedral shape (Fig. 8).

A well-defined maghémite rim directly overlies the Z2 zone. A few pyrrhotite grains have small domains with an unusual high density of Fe-oxides located directly underneath the rim. The associated vesicles are very small. The resulting polycrystalline domains are an almost pure Fe-oxide material.

L2006A28

The particle (14 × 7 × 7 μm) is a massive aggregate consisting of a large, shattered sulfide with several smaller sulfide grains and a few ferromagnesiosilica patches at the surface. The IDP diameter is 9.4 μm. The shattered angular grains range from 3.0 μm × 1.8 μm to ~1 μm. Much smaller angular grains, ~15 nm to 500 nm in size, occur in intra-granular pockets. The upper size limit of the latter is ill defined. The continuous, polycrystalline Fe-oxide rim (220–380 nm-thick) is characterized by equilibrium triple junctions among maghémite grains (Table 1) that include tetragonal maghémite indicated by 1.25 nm lattice fringes. Massive polycrystalline ferromagnesiosilica patches have sharp contacts at pyrrhotite grains. The rim on the patches has a distinct ultrafine-grained (<50 nm) layer beneath an outer layer of ~200 nm-sized Fe-oxide single-crystals. The ferromagnesiosilica material includes Al-bearing (3.3 ± 1.4 wt% Al_2O_3) and Al-free compositions that resemble those in L2005E40 (cf. Table 6, #2 and #3), plus associated, but rare, amorphous aluminosilica material with up to 9 wt% Al_2O_3. The S-free patches generally contain pores up to ~40 nm in size.

The average sulfide, $Fe_{0.83}Ni_{0.02}S$, is single-crystal low-Ni pyrrhotite (Tables 2 and 4) (Fig. 9) with an outlier, $Fe_{0.56}S$, close to the particle surface along with a 50-nm Fe, Cr-grain (chromite?). Ni-free pyrrhotite is rare. The mottled texture along the grain boundary of single-crystal grains and of the intra-granular lamellae show the onset of formation of mélanges of fine-grained pyrrhotite and Fe-oxide plates that are on average 17 nm long ($1\sigma = 6.6$). Generally, the textures resemble the mottled Z1 zone of IDP L2005E40 (Fig. 6). Domains with high Fe-oxide grain densities are rare. The development of a Z2 zone is limited to an abundance of very small, round vesicles. A layered sequence of zones is poorly developed with a few euhedral hexagonal vesicles (10–20 nm).

The sulfide-ferromagnesiosilica interactions are limited but otherwise identical in chemical zoning and texture to L2005E40. There are no lath-shaped sulfide grains but rather tabular and acicular grains <50 nm long. Embedded (sub-)circular mottled pyrrhotite grains, ~9 at% Ni (Fig. 9), range from 8 nm to 100 nm ($\mu = 37.4 \pm 19.5$ nm). High-S ferromagnesiosilica patches are in sharp contact with

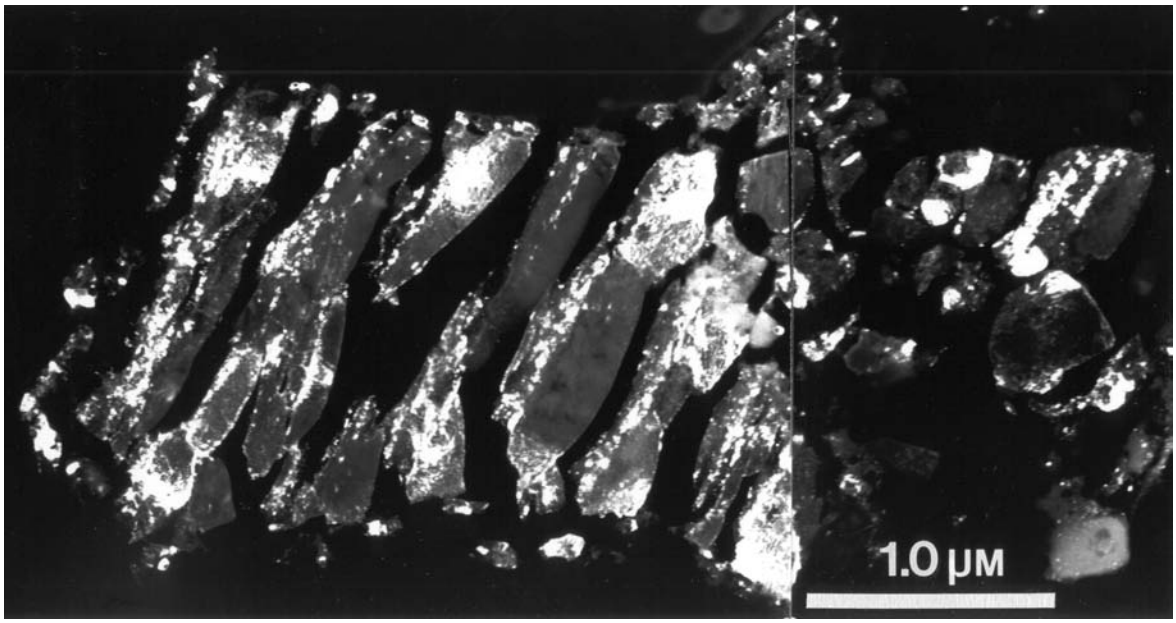

Fig. 4. Dark-field TEM image of the similar section of IDP L2005E40 (Fig. 2) but showing the mottled texture along sulfide grain boundaries; the grain interiors (dark gray) are single-crystals. An enstatite crystal (light-gray) is visible just above the scale bar.

Table 4. Comparisons of interplanar spacing values (nm) of low-Ni and high-Ni sulfides in IDPs L2005E40, L2006A28, and L2005C39 obtained by SAED analyses compared with pyrrhotite from the J.C.P.D.S. files: 24-220 (hexagonal 3C), 22-1120 (hexagonal 4C), 29-723 (monoclinic 4C), and 29-724 (hexagonal 5C).

Low Ni pyrrhotite			High-Ni sulfide				
L2005E40	L2006A28	L2005C39	L2005E40	Hexagonal 3C	Hexagonal 4C	Monoclinic 4C	Hexagonal 5C
				0.69			
0.60	0.60		0.60	0.59	0.59		
0.58	0.58	0.58				0.58	0.585
0.57	0.57			0.57	0.57	0.57	
			0.56	0.56			
		0.45		0.49			
		0.38		0.41			
			0.35	0.35	0.34	0.34	0.34
0.32				0.32		0.32	
0.31	0.31					0.31	
0.30	0.30	0.30	0.30	0.30	0.30	0.30	0.30
0.29	0.29	0.29			0.29		0.29
0.28				0.28		0.285	0.28
0.27	0.27	0.26		0.27	0.26	0.26	0.265

Table 5. Mean and standard deviation of the pentlandite sulfur and nickel content (at%) in IDP L2005E40 and high-Ni pentlandite in a "low-Ca" hydrated IDP (Tomeoka and Buseck 1984; data from this papers were reworked by the author). N: number of data.

IDP	Mean ± 1	N
L2005E40	S = 49.1 ± 2.0	30
	Ni = 21.5 ± 1.6	30
"Low-Ca" hydrated IDP	S = 47.3 ± 0.5	4
	Ni = 23.5 ± 3.5	4

pyrrhotite (Fig. 10). High-S materials and compact S-free ferromagnesiosilica patches occur individually in sharp contact with pyrrhotite. They share a sharp contact with each other in only one location. Unique intra-granular masses (100–200 nm in size) of densely packed, ultrafine pyrrhotite grains are intimately associated with pyrrhotite. Rare amorphous inclusions in pyrrhotite (Fig. 11) are almost-pure sulfur (Fig. 9). These electron beam-sensitive inclusions are found embedded at the pyrrhotite grain boundary. This IDP contains a single Ni, P-grain (175 × 87 nm; schreibersite?).

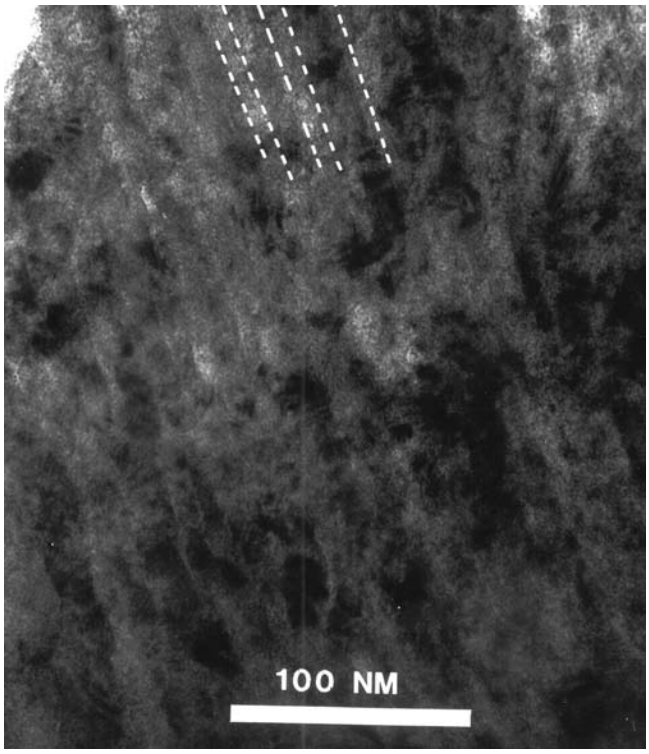

Fig. 5. TEM image showing the parallel stratification of narrow bands with a mottled texture (dark) separated by narrow amorphous bands (gray) with scattered ultrafine maghémite grains in pentlandite (Ni = 23 wt%) in a thin-section of IDP L2005E40. The white dashed lines are drawn to highlight the linear features in one are of this texture.

L2005C39

A trapezoidal particle (14 × 8 × 7.5 μm) (diameter: 9.8 μm) has a smooth surface and covered by an almost continuous, 250–500 nm-wide Fe-oxide rim (Fig. 12). The Fe-oxide is tetragonal maghémite (Table 1). Locally the rim has a layer of smaller (70–100 nm) rounded grains underneath a coarser grained (140–215 nm) exterior layer. A thinner (~45 to 140 nm) rim of euhedral maghémite grains that seems continuous with the rim on sulfides covers the knobs (0.6–1.2 μm in size) of compact polycrystalline ferromagnesiosilica material at the surface. Elongated angular grains range from 1.5 × 0.25 μm to 5.0 × 0.5 μm, but much smaller grains are common (Fig 12). The sulfide, $Fe_{0.98}S$, is single-crystal Ni-free pyrrhotite (Fig. 13; Tables 2 and 4) except in the mottled grain boundary zones. The [100] single-crystal SAED patterns of sulfide grains show vacancy ordering as indicated by the reciprocal super cell lattice rows (Fig. 14). A few grains have a $Fe_{0.85}S$ composition (Fig. 13). The Z1 zone as defined in IDP L2005E40 has few tiny (3–6 nm) round vesicles in sulfide is best developed close to the rim. Euhedral vesicles (~25 nm) are rare. There is no recognizable Z2 zone. Ferromagnesiosilica knobs with a Fe-rich serpentine dehydroxylate composition (Table 6, #4) are in sharp contact with underlying sulfide. A tabular Al-bearing diopside grain, $En_{39}Fs_{15}Wo_{46}$ (500 × 300 nm) and associated (235 × 115 nm) pigeonite grain ($En_{69}Fs_{21}Wo_{10}$) are sandwiched between sulfide and rim.

Table 6. Bulk composition (wt% oxides or element) of ferromagnesiosilica materials in reaction zone in IDP L2005E40 (1–3) and polycrystalline material on IDP L200C39 (4) (n.d: not detected).

	1	2	3	4
SiO_2	49.8	63.0	68.2	38.0
Al_2O_3	5.1	5.5	n.d.	n.d.
MgO	8.9	11.0	28.9	17.4
FeO	25.0	18.4	2.0	44.6
CaO	1.2	2.1	n.d	n.d.
MnO	0.2	n.d	n.d	n.d.
NiO	6.3	n.d	n.d	n.d.
S	3.4	n.d	n.d	n.d.

DISCUSSION

Unmelted pyrrhotite IDPs such as L2005E40, L2005C39, and L2006A28 are relatively rare among the collected stratospheric IDPs. Tomeoka and Buseck (1984) identified pyrrhotite with a hexagonal superstructure and thin (10–30 nm) euhedral low-Ni pentlandite (Ni <3 at%) plates up to ~800 nm long with a mosaic texture in a "low-Ca" hydrated IDP. Large sulfides in cluster IDPs contain small inclusions and embayed grains of feldspathic glass (albite?), Ca, Si, Mg-rich material (diopside?), olivine, Mg-rich pyroxene, sphalerite, rare Cr-rich grains (chromite?) and kamacite, and have loosely adhered aggregate material (Brownlee et al. 1989; Schramm and Brownlee 1990). This mineralogy resembles what is found in the sulfide IDPs presented here. Large (10–25 μm) sulfide and silicate grains and grain clusters with still attached aggregate material are found occasionally on dust collectors in intimate association with aggregate fragments that resemble 10–15 μm chondritic aggregate IDPs. Brownlee et al. (1977) already noted that such associations were caused during inertial-impact collection by the break-up of large cluster IDPs.

In a study of Fe- and Fe, Ni-sulfides, Zolensky and Thomas (1995) concluded that Ni-rich Fe-sulfides, including pentlandite, are only present in hydrated chondritic IDPs. When correct, this observation has implications for the origins of chondritic aggregate and cluster IDPs because a dogmatic believe holds that dust hydration could only occur in asteroids and dust hydration in comet nuclei cannot happen. Specifically hydration refers primarily to layer silicate formation in anhydrous precursor silicate materials (crystalline or amorphous), while embedded sulfides and silicate minerals may remain unaffected. Thus, by this argument anhydrous IDPs can never contain Ni-rich sulfides and yet the formation of such sulfides is not much understood. There is also a notion that fluffy particles have a cometary

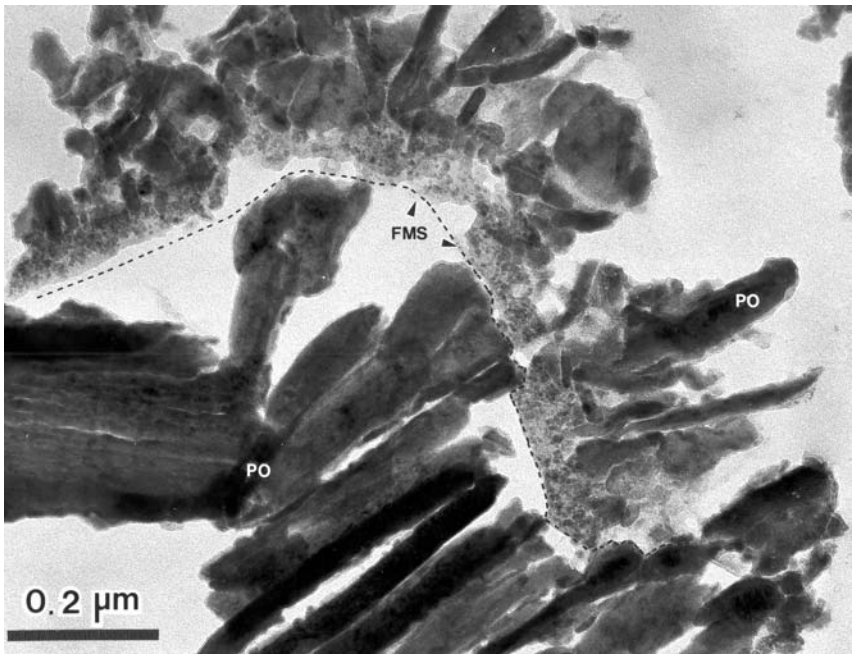

Fig. 6. TEM image of a microtomed thin-section of IDP L2005E40 showing pyrrhotite laths (po: lower-left part) from the original sulfide in a sharp contact (black dashed line) with ferromagnesiosilica (FMS) material with embedded angular and rounded pyrrhotite grains (dark gray) and enclosing smaller pyrrhotite plates and laths (po) towards the exterior part of this structure. The Fe-oxide rim is not shown in this image. The dark gray background is the embedding epoxy; the lighter gray area "enclosed" within the dashed black line indicates loss of shattered pyrrhotite material.

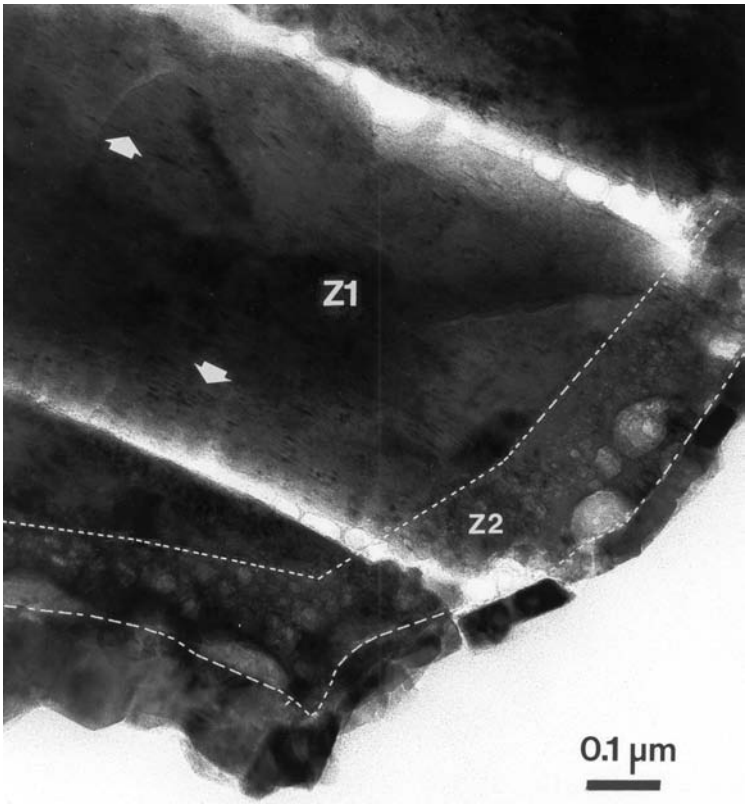

Fig. 7. TEM image of a microtomed thin-section of pyrrhotite in IDP L2005E40 showing the mottled Z1 zone with variable density of Fe-oxide plates oriented parallel to the host (100) (white arrows), the Z2 zone with abundant small vesicles (gray) with larger ones immediately below the Fe-oxide rim. The white dashed lines delineate the zones. The grayish material in both fractures is the embedding epoxy.

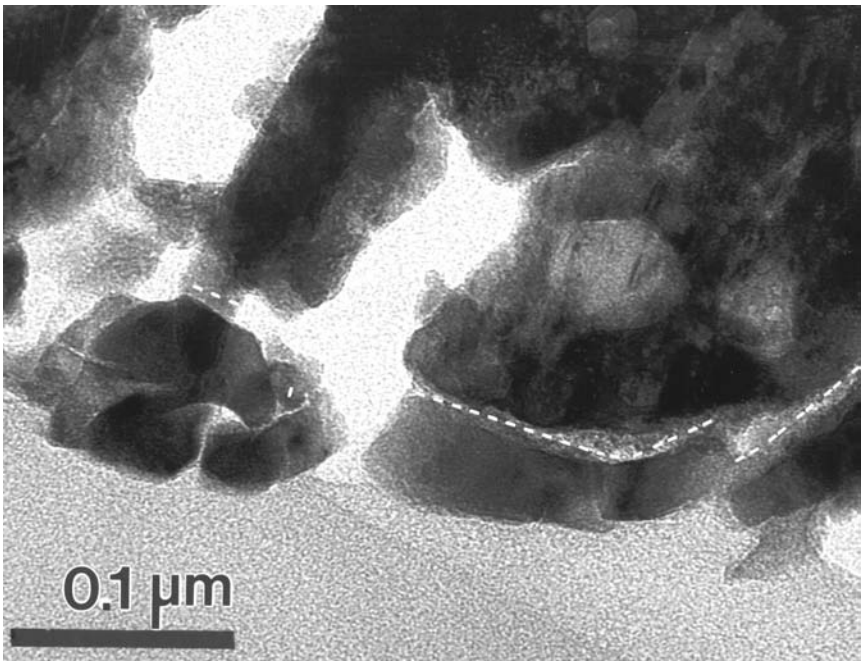

Fig. 8. TEM image of vesicular pyrrhotite in a microtomed thin-section of IDP L2005E40 showing a large vesicle with a regular outline in the Z2 zone underneath the Fe-oxide rim delineated by the white dashed line. The dark gray background is the embedding epoxy; the supporting holey carbon thin-film is the light gray background.

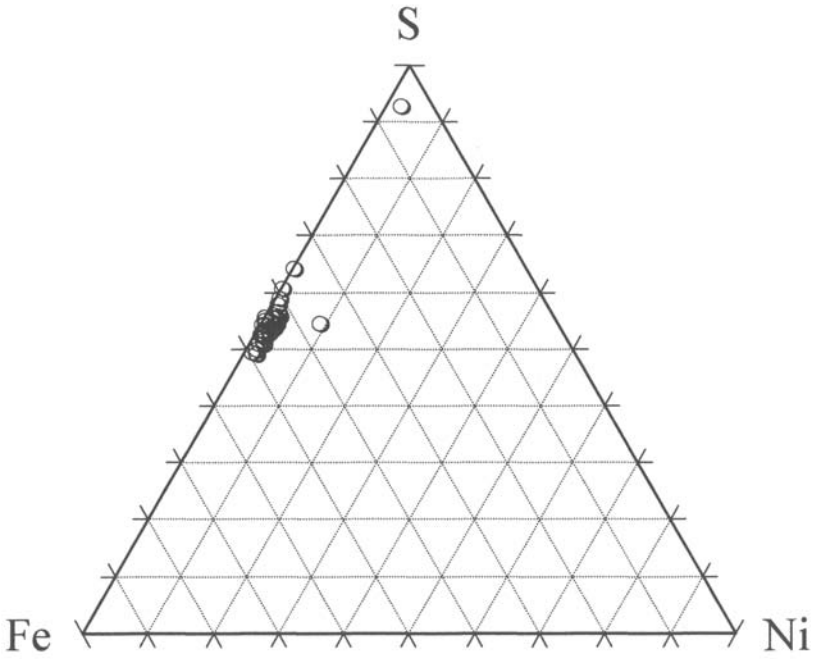

Fig. 9. Sulfide compositions in IDP L2006A28 plotted in the ternary Fe-Ni-S (at%) system.

origin while compact or smooth IDPs are from asteroids. Almost intuitively indeed, the fluffy IDP morphology suggests a link to ice-rich parent bodies. In the wake of the comet Halley encounters, the best matches for the observed Halley dust properties were made with fluffy aggregate IDPs (Lawler and Brownlee 1992; Rietmeijer 2002a). Does it mean there could be no aggregate and larger cluster IDPs in asteroids? Apparently not, according to Thomas et al. (1995) who described an asteroidal cluster IDP. The conclusion of Zolensky and Thomas (1995) critically depends on the

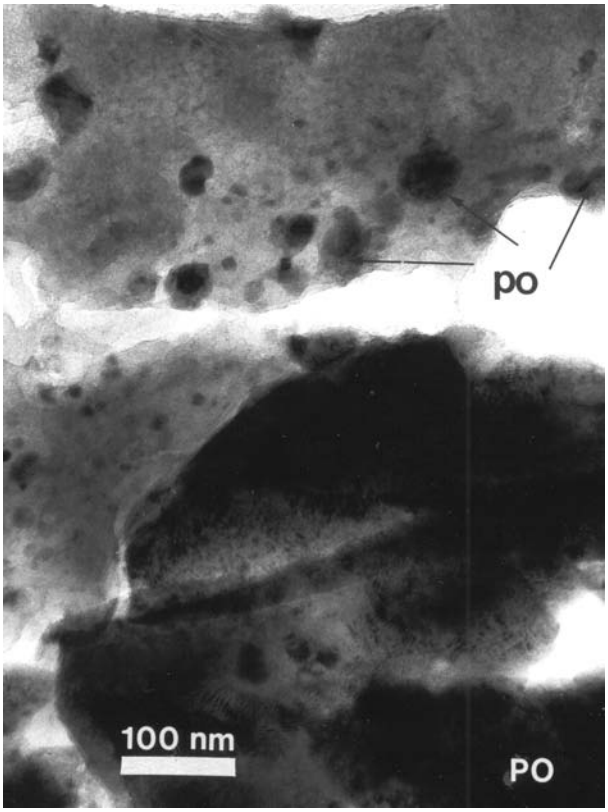

Fig. 10. TEM image of a microtomed thin-section of IDP L2006A28 showing (sub-)circular mottled pyrrhotite grains (po; black) embedded in high-S ferromagnesiosilica material in contact (sub-parallel to the plane of the section) with pyrrhotite (po; white); the opaque grains in the lower right-hand corner. White spaces are ruptures in the IDP section.

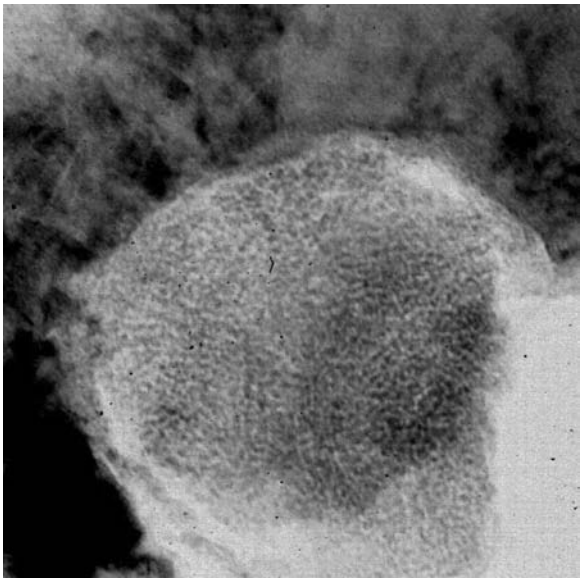

Fig. 11. TEM image showing an amorphous, almost pure sulfur inclusion in a mottled pyrrhotite grain in IDP L2006A28. This round inclusion is 120 nm in diameter. The background shows the holey carbon support thin-film

assumption that hydration would be a unique asteroid phenomenon, pervasive throughout the asteroid belt, including the outer P- and D-infrared asteroids, and the comet-like near-Earth asteroids. However, traces of layer silicates were probably present in Halley dust (Rietmeijer et al. 1989), minor amounts layer silicates are present in porous aggregate IDPs (Rietmeijer 1991; Rietmeijer and Mackinnon 1985a) and meteors with CI-like physical properties enter the Earth's atmosphere on comet-like orbits (Rietmeijer 2000) offering ample support that hydrated aggregate IDPs, cluster IDPs, and even larger aggregate debris is associated with cometary sources. Hydrocryogenic alteration in dirty-ice mixtures (Rietmeijer 1985, 2002a) and laboratory hydration experiments on amorphous MgSiO dust analogs (Rietmeijer et al. 2004) provide a framework supporting the feasibility of dust hydration in cometary environments.

The original subdivision of anhydrous and hydrated IDPs was based on the findings of an infrared study of 26 chondritic IDPs. When a featureless 9.8-μm band that was considered to be characteristic for phyllosilicate minerals dominates the IR spectrum the particle was classified as a hydrated IDP (Sandford and Walker 1985). TEM analyses of two IDPs showing this hydration IR feature signature had found abundant layer silicates along with unaltered sulfides and silicates (Sandford and Walker 1985). Zolensky and Barrett (1994) in their study of olivine and pyroxenes in chondritic IDPs re-defined "hydrated" to mean that any amount of layer silicates however miniscule would justify a hydrated IDP classification. It is of course entirely correct but in this manner they were able to conclude that Ni-bearing Fe-sulfides are limited to hydrated IDPs. They ignored the fact that the hydrous signature was linked to the silicate materials only. When water react with silicates in anhydrous IDP the extent of hydration will be a function of water/"rock" ratios, time and temperature of hydration as well as the ability of water to move through a porous medium. Laboratory hydration of a porous condensed MgSiO smoke demonstrated that porosity is indeed an important controlling factor during hydration (Rietmeijer et al. 2004). The most likely outcome of the hydration process would be a continuous and gradual transition from anhydrous silicates (crystalline or amorphous) to partially and to fully-hydrated silicates among aggregate IDPs that can be from the same parent body or from different parent bodies. Unless, it can be demonstrated that "anhydrous" and "hydrated" minerals in extraterrestrial materials were both the result of a primary dust-forming process (e.g., condensation), classification of IDPs as hydrated and anhydrous is nonsensical. When this is not the case a classification, especially one with genetic overtones, cannot mix primary and secondary particle properties such as hydration.

The chemistry, petrology, and mineralogy of chondritic IDPs support a primary subdivision of IDPs as either non-

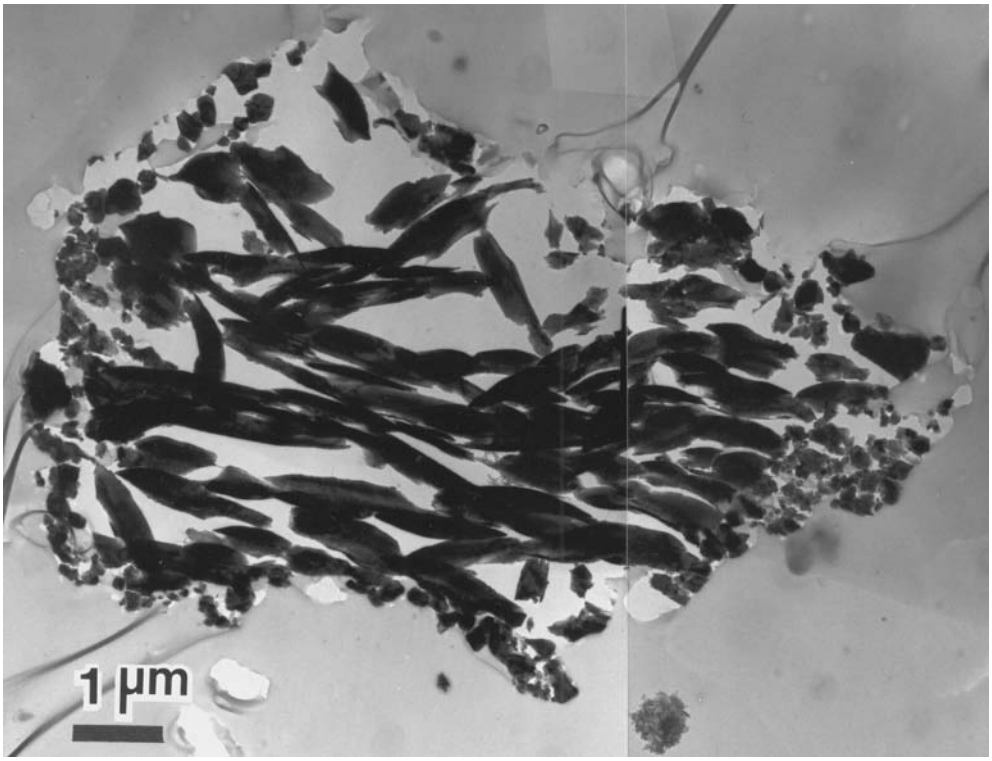

Fig. 12. TEM image of an ultramicrotomed section of sulfide IDP L2005C39 showing its brittle behavior during sectioning causing disconnected elongated angular grains and sample material loss (light gray background with the sample area). The distinctly smaller equant grains along the perimeter are Fe-oxide grains from the rim on this IDP. The dark gray background surrounding the IDP slice is the embedding epoxy (the spherical particle at the bottom, right, is a dust particle on the negative.

chondritic or chondritic, with chondritic IDPs being either non-aggregate IDPs or aggregate IDPs; properties that readily determined by TEM analysis. The chondritic non-aggregate IDPs tend to have a CI or CM affinity, the chondritic aggregate IDPs range from fully anhydrous to partially hydrated and to fully hydrated IDPs wherein all of the original silicates were replaced by layer silicate minerals and may be accompanied by other secondary phases, e.g., sulfates and carbonates (Rietmeijer 1998). As long as the cause and effect relationship between silicate hydration and Ni-content of Fe-sulfides in the same aggregate IDP or cluster IDP is not established the relationship reported by Zolensky and Thomas (1995) should be considered to be a tenuous one at best. The hierarchical dust accretion hypothesis recognizes a fractal property of primitive solar nebula dust aggregates whereby a limited number of dust types is recycled through multiple sequences of dust accretion—protoplanet modification (including dust grain growth)—protoplanet disruption—evolved dust accretion (Rietmeijer 1998, 2002a) rather than monotonous nebula dust accretion. This hypothesis predicts that dust accretion and dust hydration will be uncorrelated events. It seems highly premature to exclude the possibility that Ni-rich Fe-sulfides, including pentlandite, such as IDP L2005E40 could not exist in comet nuclei. The observed Ni, Cr, V, and Co abundances in some sun-grazing comets would support that sulfides, unidentified but probably Ni-bearing, and oxides are present in at least some comets (Rietmeijer 1988).

Sulfide Heating and Oxidation

Synchrotron XRD analyses of pyrrhotite in two chondritic IDPs gave Laue patterns indicating twinned pyrrhotite (3C) in L2005AE6 and pyrrhotite (3C) plus magnetite in L2005AG17 (Ohsumi and Zolensky 1998), which are similar to hexagonal pyrrhotite (3C) and Fe-oxides in the sulfide IDPs L2005E40, L2005C39, and L2006A28 from the same collector. The results are also consistent with the observation that oxygen in natural hexagonal and monoclinic pyrrhotite is not in solid solution at room temperature, but is overwhelmingly present in fine magnetite inclusions (Graham and McKenzie 1987).

Kübler (1982) described a continuous composition gradient over distances of 12–14 μm in a "monocrystalline" terrestrial pyrrhotite specimen with decreasing Fe content from the specimen interior to cleavage planes that are covered by a Fe-oxide layer. Roasting of this natural pyrrhotite in the presence of oxygen produced a 500 nm-thick oxide layer on the specimen and established a continuous Fe gradient between 254–308 °C in high-temperature disordered hexagonal pyrrhotite that reverted to low-temperature monoclinic (4C) and hexagonal (5C) pyrrhotite (Kübler

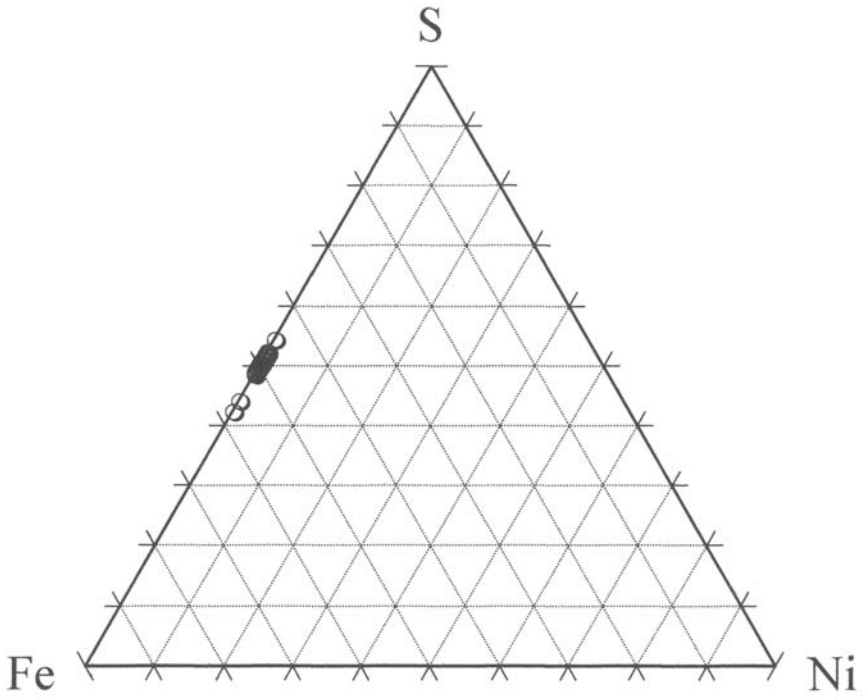

Fig. 13. Ni-free pyrrhotite compositions in IDP L2005C39 shown in the ternary Fe-Ni-S (at%) system; the two low-S compositions were obtained close to the Fe-oxide rim and might be contaminated analyses.

1982). Kübler (1982) noted that non-stoichiometric pyrrhotite would be Fe-deficient due to sulfide vacancy formation and iron oxidation. The pyrrhotite compositions in IDPs L2005E40 and L2006A28 extend up to greigite (Fe_3S_4; 59–64 S at%). In all three sulfide IDPs, pyrrhotite has a mottled texture due to unit cell variations as a function of variable Fe/S ratio, temperature and in situ formed nanocrystalline Fe-oxides.

It will be germane to the discussion to make three general observations. First, all three non-chondritic IDPs have an Fe-oxide rim and disseminated Fe-oxide grains in the interior, which proves they are extraterrestrial debris that was flash-heated during atmospheric entry (Fraundorf 1981; Flynn 1994; Rietmeijer 1998). Second, there is a consensus that extraterrestrial Fe-sulfides are products of condensed metallic FeNi sulfidation by H_2S gas within circumstellar nebulae, e.g., the solar nebula (Lauretta et al. 1996; Llorca and Casanova 2000; Meibom et al. 1999; Zolensky and Thomas 1995). This unique origin should be considered in studies of thermally processed extraterrestrial sulfides. That is, the geological Fe-Ni-S phase relations that assume an equilibrium vapor (e.g. Kullerud et al. 1969) have limited use to constrain the sulfide relationships in IDPs, except perhaps sulfides due to parent body processes. It is unlikely that an equilibrium sulfur vapor would have existed during atmospheric entry to define sulfide phase relationships. Third, the physical conditions of dynamic pyrometamorphism favor the kinetically controlled formation of metastable phases.

Brittle Sulfides

The nature of the process that caused the formation of pyrrhotite laths and the remnant angular grains in ferromagnesiosilica patches is not clear. The convergence of Ni-contents of pentlandite and pyrrhotite and the pyrrhotite-like pentlandite unit cell clearly indicate that the IDPs were heated, but whereby the duration of the heating event was not a controlling factor (Likhachev and Brauer 1969). A stratified Fe-oxide rim was also observed in a flash-heated CM-type IDP (Rietmeijer 1996c) suggesting that this phenomenon has a common cause in many IDPs. At the ultra-rapid flash heating and quenching rates of IDPs, rapid volume expansion and contraction might have structurally weakened the sulfide IDPs, but the efficiency of this process to shatter pyrrhotite and pentlandite grains is unknown. It is possible, but not likely, that space weathering from impacting energetic nuclei on a parent body and/or during solar system sojourn might have structurally weakened sulfides to a point where they would break apart during atmospheric entry heating. No characteristic features, e.g., solar flare tracks, pointing to such interactions were found. Of course, solar fare tracks could have been erased during flash heating. Radiation-induced amorphization (Flynn 1996; Rietmeijer 1999; Zolensky et al. 2003) might have produced the amorphous lamellae in pentlandite of IDP L2005E40. Whatever process was responsible to cause the brittle behavior and shattering of sulfides, it predated the time of ferromagnesiosilica melting

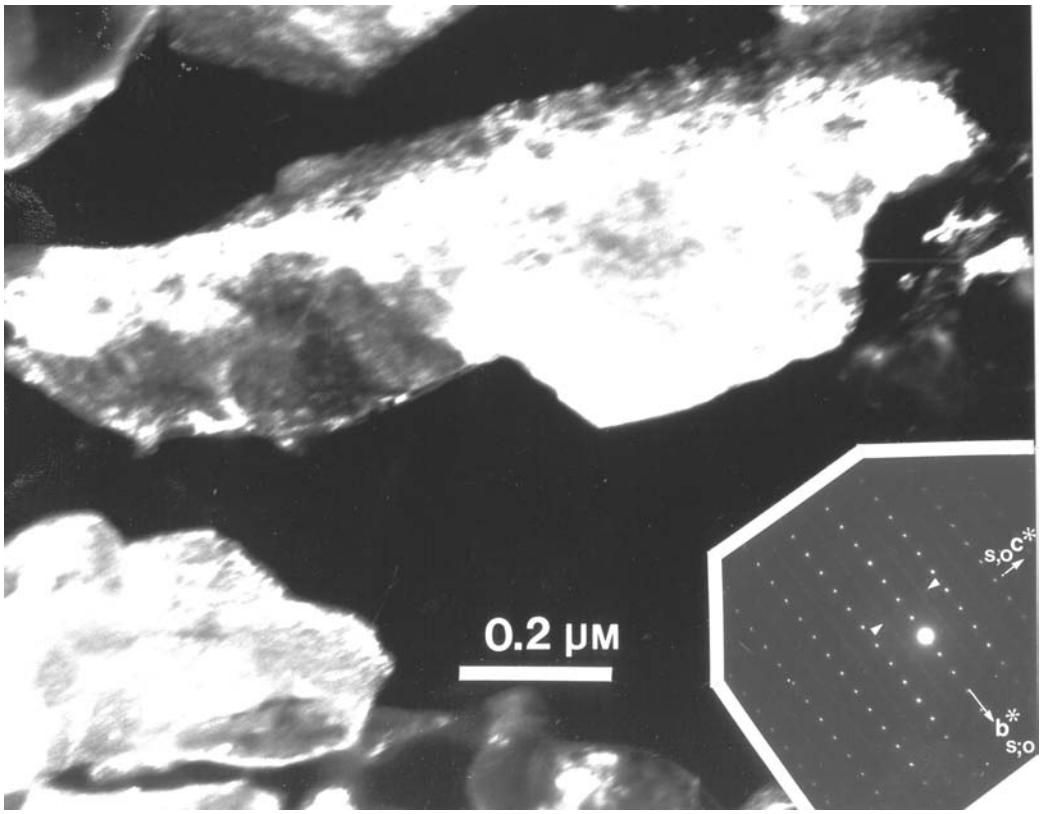

Fig. 14. Dark-field TEM image of three mottled pyrrhotite single-crystal grains in IDP L2005C39; the [100] zone axis SAED pattern of the grain in the center of the image (inset) shows the reciprocal lattice rows (white arrows) due to vacancy ordering in between the pyrrhotite pattern.

because angular fragments were embedded in and eroded by this silicate melt. The simplest explanation would be impact-related sulfide fracturing and comminution when the sulfide IDPs resided in or were ejected from the parent body or bodies.

Vesicular Sulfides

Vesicles have been reported in (unspecified) hydrocarbons (Rietmeijer 1998), olivine (Rietmeijer 1996b), diopside (Rietmeijer 1999) and sulfides (Brownlee et al. 1998; Rietmeijer 1996c) in a number of IDPs. The vesicles in volatile hydrocarbons quickly developed during exposure to the incident electron microbeam, but not in olivine and sulfides. Crystallographically aligned voids are abundant in olivine from a thermally metamorphosed carbonaceous chondrite (Akai 1994). Voids ("bubbles") were experimentally produced in terrestrial pyrrhotite that was heavily irradiated with 4 keV He ions (Brownlee et al. 1998). Heavy irradiation is the most likely process responsible for vesicles in sulfides and olivine in aggregate IDPs when bubbles nucleated on irradiation-induced lattice defects and vacancies. An irradiation-related origin for vesicles in the large sulfide IDPs cannot be excluded. However, the sulfide textures that developed during flash-heating have a correlation between sulfide oxidation, Fe-oxide formation and sulfur gas loss. Accepting that lattice defects could act as nucleation sites for sulfur vapor, I note that single-crystal pyrrhotite in IDP L2005C39 and in the other two IDPs, albeit much less obvious, show vacancy ordering (Fig. 14).

Sulfide Oxidation and Sulfur Loss

The sulfide compositions (Figs. 3, 9, and 13) and crystallographic and textural properties suggest a sequence of reactions during flash heating and subsequent ultrafast quenching in the large Fe, Ni-sulfide IDPs. They were 1) sulfide oxidation and 2) sulfide decomposition and Fe-oxide formation, both leading to S-loss. I adopt the experimentally determined iron and sulfur self-diffusion model by Condit et al. (1974) describing iron oxidation in non-stoichiometric hexagonal and monoclinic pyrrhotite, expressed as hexagonal $Fe_{1-\delta}S$, as a function of temperature. The model incorporates the effects of iron oxidation and vacancy ordering in Fe-sulfides with a NiAs structure that allows the withdrawal of an appreciable amount of iron atoms from structural sites (Condit et al. 1974). It involves either formation of electron holes or Fe^{3+} formation when these holes are located on specific iron sites to compensate for the withdrawal of iron from the sulfide structure. The changes are described by a compound formula,

$^{2+}Fe_{1-3\delta}{}^{3+}Fe_{2\delta}\square_{\delta}S$, where $\square$ is an iron vacancy and δ is the iron deficit (Condit et al. 1974). For example, δ = 0.12 in pyrrhotite (Fe/S = 7/8) corresponds to 27% Fe^{3+}. The maximum possible δ value would be 0.33 for a "sulfide," wherein all iron is trivalent. In reality the maximum occurs for greigite with δ = 0.25 corresponding to ~65% Fe^{3+} for hexagonal pyrrhotite at ~1,050 °C (Condit et al. 1974, Fig. 2). In this model, the S_2 (gas) partial pressure between ~10^{-9} and ~0.1 bar will determine the extent of $Fe_{1-\delta}S$ pyrrhotite formation between ~400 °C to ~700 °C as a function of increasing δ and temperature.

The average non-stoichiometric pyrrhotite compositions (Table 2) indicate an average δ value of 0.22 (L2005E40; L2006A28), and 0.02 (L2005C39) with the full range in this IDP up to δ = 0.15 with Fe^{3+} up to 100% (Table 7). For the dominant pyrrhotite composition in the sulfide IDPs (δ = 0.15; Table 7), the compound formula $^{2+}Fe_{0.55}{}^{3+}Fe_{0.30}\square_{0.15}S$ (35% Fe^{3+}) is close to Fe_7S_8. Oxidation of the highest possible oxidized pyrrhotite in the model (Condit et al. 1974) can be written as $2(^{2+}Fe_{0.25}{}^{3+}Fe_{0.5}\square_{0.25}S) + 0.75\ O_2 = 0.5\ Fe_2O_3 + 0.5\ FeS_2 + 0.5\ S_2$ (liquid; gas), wherein the ordered vacancies in the *bc* plane, as seen in terrestrial pyrrhotite (Posfai et al. 2000), were sites for crystallographically controlled growth of Fe-oxide plates and vesicles in IDP L2005C39. Support for this reaction comes from FeS_2-like sulfide and almost pure sulfur (quenched liquid or vapor) compositions in IDP L2006A28 (Fig. 9). Should liquid sulfur vaporization have been fast enough, pyrrhotite decomposition might have followed the one-step release of a S_2 molecule as was experimentally verified by Hong and Fegley (1997) during pyrite decomposition.

Kinetic rather than thermodynamic equilibrium reactions during dynamic pyrometamorphism of the sulfide IDPs could have allowed the formation of a fully oxidized sulfide, $^{3+}Fe_{0.66}\square_{0.33}S$ that, upon continued oxidation, resulted in the formation of the very high density Fe-oxide zones in pyrrhotite in the heated sulfide IDPs according to a reaction, $2(^{3+}Fe_{0.66}\square_{0.33}S) + 0.99\ O_2 = 0.66\ Fe_2O_3 + S_2$ (gas). For fully oxidized sulfide formation, the Fe-S phase diagram indicates an upper limit of 10^{-5} bar for S_2 gas partial pressure.

Depending on the partial S_2 gas pressure the Fe-S phase diagram predicts that pyrrhotite with δ >0.2 decomposes to hexagonal pyrrhotite + pyrite below ~700 °C, while above ~700 °C hexagonal pyrrhotite and liquid coexist (Condit et al. 1974). Decomposition as $1.25(^{2+}Fe_{0.25}{}^{3+}Fe_{0.5}\square_{0.25}S = {}^{2+}Fe_{0.55}{}^{3+}Fe_{0.30}\square_{0.15}S + 0.0275\ FeS_2 + 0.0975\ S_2$ (gas) whereby greigite decomposes to pyrrhotite + pyrite will critically depend on the relative partial pressure of S_2 during sulfide IDP degassing and the atmospheric oxygen pressure at altitude. Both are probably low but depending on the ability to develop vesicles for sulfur loss the S_2 pressure could build up as a function of time during flash heating to the peak-heating temperature. Assuming for the moment that pyritic sulfide formed as described above during flash heating of the sulfide IDPs, subsequent low-temperature (<500 °C) pyrite decomposition could yield hematite plus SO_2 (Hong and Fegley 1997).

Table 7. Average and range of iron deficit (δ; no Ni) and percent Fe^{3+} of non-stoichiometric pyrrhotite in the sulfide IDPs L2005E40 (the outlier composition is almost FeS_2), L2006A28 and L2005C39.

	δ (average and range)	% Fe^{3+} (average and range)
L2005E40	0.15 (0–0.37)	35 (0–100)
L2006A28	0.17 (0–0.33)	41 (0–100)
L2005C39	0.02 (0–0.15)	4 (0–35)

Experimental studies (Condit et al. 1974; Hong and Fegley 1997) offer a coherent framework for crystallographically controlled formation of Fe-oxides and vesicles, a double Fe-oxide rim of different grain sizes, and the range of pyrrhotite compositions established during atmospheric entry of the sulfide IDPs described here. In nm- to micron-sized grains of these particles diffusion is not a rate-controlling process. This is consistent with the experimentally determined sulfur and iron self-diffusion rates in sulfides (Condit et al. 1974; Hong and Fegley 1997). Iron-oxide formation including rims on sulfide IDPs L2005E40, L2005C39, and L2006A28 involved only solid-state processes without any loss of iron. These IDPs lost sulfur and acquired terrestrial oxygen. Subdivided as a function of time during dynamic pyrometamorphism (5–15 s; Love and Brownlee 1991), ferrous pyrrhotite oxidation occurred when temperatures rose to peak heating, while formation of Fe-oxides and major loss of sulfur occurred at and after maximum heating during ultra-fast quenching.

Silicate Materials

The ferromagnesiosilica materials mostly at the surface of the sulfide IDPs are flash-melted pockets. This is highlighted by the S-free, porous aggregate, patches on IDP L2006A28. This particular porous structure does not appear to be a gas-release feature but rather due to thermal annealing of a porous aggregate precursor as was observed developing during thermal annealing and grain coarsening of condensed porous magnesiosilica smokes (Rietmeijer et al. 2002). Hydration of the same smoke sample showed that hydration tends to collapse the originally anhydrous, porous smoke into a dense hydrated MgSiO-material with a disappearance of any traces of the highly porous original smoke (Rietmeijer et al. 2004). This finding is consistent with the observation that hydrated IDPs tend to have a relatively uniform texture of low porosity (Bradley 1998). These experimentally-produced annealing and hydration textures are sufficiently unique that, with a fair degree of certainty, it can be concluded that the attached ferromagnesiosilica materials were anhydrous aggregates and not "collapsed" hydrated saponite and

serpentine materials. It is then unlikely that the observed ferromagnesiosilica compositions are the result of layer silicate dehydration for example during atmospheric entry flash heating. The Al, Ca-bearing ferromagnesiosilica materials in L2005E40 and L2006A28 have smectite dehydroxylate compositions that are identical to coarse-grained principal components in the matrix of aggregate IDPs (Rietmeijer 1998, 2002a; Rietmeijer et al. 1999). The serpentine dehydroxylate composition of Fe-rich ferromagnesiosilica material in L2005C39 is identical to ultrafine-grained PCs in aggregate IDPs (Rietmeijer 2002a). Such dehydroxylate compositions formed by mixing vapor-condensed amorphous silicate grains with preferred metastable eutectic composition (Rietmeijer 2002a; Nuth et al. 2000, 2002), including amorphous aluminosilica material in L2006A28 with a metastable eutectic aluminosilica composition (Rietmeijer and Karner 1999). The basic physical conditions behind this metastable behavior expressed as distinct and predictable solid compositions are 1) high initial temperature and 2) ultra-rapid quench rates form either a vapor of a high-temperature liquid (Rietmeijer et al. 2000). The smooth shapes of the materials attached to the sulfide IDPs described here suggest flash melting and ultra-rapid quenching rather than evaporation.

In L2005C39 and L2006A28, the contacts between ferromagnesiosilica patches and pyrrhotite are mostly sharp without any evidence of chemical zoning across the interface. It is different in L2005E40, and to a much lesser extent in L2006A28, where relic grains of angular, lath-shaped and rounded pyrrhotite are embedded in ferromagnesiosilica material. The relic grain size distributions point to assimilation of the smallest sulfide grains, which is supported by the S-content of the ferromagnesiosilica materials. This is the only evidence for melting in these sulfide IDPs and it only affected the adhered ferromagnesiosilica materials. The metastable compositions unambiguously support ultra-fast quenching of the sulfide IDPs. The metastable nature of the amorphous "silicate" compositions prohibits using equilibrium phase relations to establish their dynamic, peak-heating metamorphic temperatures.

Dynamic Pyrometamorphism Temperatures and IDP Sources

Previously, Rietmeijer (1992) argued that a thermal gradient develops in sulfides during flash-heating because Fe-sulfide oxidation, $2\ FeS + 3/2\ O_2 = Fe_2O_3 + 2\ S$ (gas), is endothermic below ~525 °C due a positive enthalpy (~380 Kcal mol^{-1}, JANAF) of mono-sulfuric gas. However, pyrite decomposition experiments showed that not only would the nature of released sulfur allotropes affect the overall energy distribution of the decomposition process, the efficiency of vaporization of liquid sulfur produced would also be critical (Hong and Fegley 1997). The vesicular pyrrhotite textures and correlation of vesicle size with increasing Fe-oxide formation suggest that efficient pathways for loss of sulfur existed during flash-heating of sulfur IDPs described here. The modification features in these IDPs should not be taken in support of a thermal gradient.

What thermal indicators are available for the sulfide IDPs? The pyrrhotite-like unit cell data for pentlandite in L2005E40 and the sulfide compositions suggest that this particle was heated at least to >250–300 °C (Likhachev and Brauer 1969). To achieve the same features at higher heating rates in this IDP compared to the experiments, actual dynamic metamorphic temperatures had to be much higher (Rietmeijer and Mackinnon 1985b). A potentially better thermometer would be the stability of non-stoichiometric, iron-deficient δ, hexagonal pyrrhotite in the Fe-S phase diagram (Condit et al. 1974). The maximum temperature in L2005E40 and L2006A28, using data from Table 7, is estimated at ~700 °C. It is probably also a fair estimate for L2005C39. The estimate is made without knowledge of the S_2 gas partial pressure, or more accurately its evolution during ultra-fast heating and quenching. Co-existing pigeonite and diopside in IDP L2005C39 suggest a maximum temperature indicated by the solidus phase relationships in the pyroxene quadrilateral between 1300 and 1350 °C although the presence of Al_2O_3 might lower these temperatures by 100–200 °C (Huebner and Turnock 1980). The best estimate of the peak-heating temperature in sulfide IDPs L2005E40, L2006A28, and L2005C39 is ~700 °C.

The peak heating temperature of an IDP is an indication for its entry velocity using a matrix developed by Love and Brownlee (1994) for particles between 2 and 50 μm in diameter with a density of 2 g/cm^{-3} and a 45° entry angle that covers average conditions for most of the incoming IDPs. Taking a 9-μm diameter for L2005E40, L2006A28, and L2005C39 and a peak heating temperature of 700 °C, the corresponding entry velocity is 10 km/s^{-1}; in the (unlikely) case of vertical incidence the peak heating temperature was ~825 °C. At entry angles <45°, the peak heating temperature of 700 °C at 10 km/s^{-1} would drop considerably. In this case, this peak temperature would be reached at a higher IDP entry velocity. Assuming the sulfide IDPs decelerated as individual particles, the 10 km/s^{-1} entry velocity would point to asteroidal debris. Should the peak-heating temperature have been closer to the pyroxene solidus temperature for the sulfides IDPs entering at a shallow angle, the entry velocity might have been as high as 16 km/s^{-1}. At this velocity these IDPs could be from a "particle swarm" such as the annual Andromedids shower (P/comet Biela) with a 16.5 km/s^{-1} entry velocity. Sulfide IDPs L2005E40, L2006A28, and L2005C39 most likely belonged to a cluster IDP. Thus, peak-heating to ~700 °C would point to sources that release debris at "low-velocity comet" speeds (Rietmeijer 2000) such as near-Earth and Earth-crossing asteroids that include extinct and dormant comet nuclei, e.g., Phaethon and C/2001 OG108 (LONEOS)

(Abell et al. 2003). A shock origin for the comminuted sulfide IDPs would exclude periodic comets as a source.

STARDUST and Astromineralogy

Comet Halley showed a dearth of sulfides (Jessberger et al. 1988). When considering the mass of dust analyzed by the on-board mass spectrometers, it follows that Halley dust was sampled at the level of the grains in the matrix of aggregate IDPs, i.e., mostly principal components up to several hundreds of nm (Rietmeijer 2002a). We do not know how many sulfide and silicate grains occur at this level of hierarchical dust accretion but such grains would be a fraction of individual dust grains in this size range (Rietmeijer 2002a). The mass spectrometers on-board the Giotto and Vega spacecraft to comet Halley could not detect micron-sized dust. As a result many of the sulfide grains in chondritic aggregate IDPs would not have been detected at this comet, let alone particles such as sulfide IDPs L2005E40, L2006A28, and L2005C39. Leonid meteor light curve morphologies (Murray et al. 2000) indicate that large massive grains that could be sulfide, silicate, or both (Rietmeijer 2000, 2002b) co-exist with large cluster IDP-like aggregates in comet Tempel-Tuttle and other comets. The STARDUST mission will be a milestone that could collect ≥10 μm stoichiometric pyrrhotite and pentlandite from an active comet to further define the hypothesis of hierarchical dust accretion beyond collectable cluster IDPs (Rietmeijer 1998, 2002a). Keller et al. (2002) proposed that a broad feature at ~23.5 μm in the Infrared Space Observatory (ISO) spectra for proto-planetary disks indicates the presence of sulfides. To reach this conclusion they compared ISO spectra with spectra of pyrrhotite grains in collected IDPs. Yet all IDPs, including their constituent sulfides, experience flash heating (Dai and Bradley 2001). The present results that show vacancy formation and sulfide oxidation during flash heating should be considered when making such spectral comparisons between flash-heated pyrrhotite and sulfides in proto-planetary disks and other environments around young stellar objects (YSOs). Alternatively, when the comparison holds firm, vacancy ordering in irradiated pyrrhotite and subsequent Fe-oxide formation should be considered in dust evolution around YSOs.

CONCLUSIONS

It is amazing what happened in the few seconds available for dynamic pyrometamorphism of Ni-free and low-Ni pyrrhotite and pentlandite that make up the IDPs L2005E40, L2006A28, and L2005C39. The data support ferrous sulfide oxidation with vacancy formation and ordering and Fe-oxide formation and sulfur gas loss in zoned arrangements of increasing levels of modification from the grain interior to the grain boundary and, on the larger scale, towards the IDP surface. Solid-state processes defined almost all thermally induced changes including formation of a continuous maghémite rim. That is, the grains of the fine-grained part of a multiple Fe-oxide rim re-crystallized into larger grains and grain coarsening occurred in the dense packed Fe-oxide domains in the fully oxidized parts of non-stoichiometric pyrrhotite. The coarser grained rim involved pyrrhotite oxidation and sulfur loss. Melting of metastable aggregates at the IDP surface produced dense patches of ferromagnesiosilica material that assimilated the smallest pyrrhotite fragments. The peak-heating temperature of ~700 °C suggests an asteroidal origin, but if the three sulfide particles belonged to a cluster IDP, the data would support the higher entry velocity of near-Earth asteroids that may include extinct and dormant comet nuclei. A possible shock-related origin for comminuted sulfides rules out an origin among active comet nuclei.

Acknowledgments–The work was performed at the Electron Microbeam Analysis Facility in the Department of Earth and Planetary Sciences (UNM) where Fleur Rietmeijer-Engelsman and Jim Karner provided technical support. I thank Mike Zolensky and David Joswiak for constructive reviews. This work was supported by grant NAG5–11762 from the National Aeronautics and Space Administration.

Editorial Handling—Dr. Donald Brownlee

REFERENCES

Abell P. A., Fernandez Y. R., Pravec P., French L. M., Farnham T. L., Gaffey M. J., Hardersen P. S., Kusnirak P., Sarounova L., and Sheppard S. S. 2003. Physical characteristics of asteroid-like comet nucleus C/2001 OG108 (LONEOS) (abstract #1253). 34th Lunar and Planetary Science Conference. CD-ROM.

Akai J. 1994. Void structures in olivine grains in thermally metamorphosed Antarctic carbonaceous chondrite B-7904. *Proceedings of the NIPR Symposium on Antarctic Meteorites* 7: 94–100.

Alexander C. M. O. D, Barber D. J, and Hutchison R. 1989. The microstructure of Semarkona and Bishunpur. *Geochimica et Cosmochimica Acta* 53:3045–3057.

Bradley J. P. 1988. Analysis of chondritic interplanetary dust thin sections. *Geochimica et Cosmochimica Acta* 52:889–900.

Bradley J. P. 1994. Chemically anomalous, pre-accretionally irradiated grains in interplanetary dust from comets. *Science* 265: 925–929.

Bradley J. P., Keller L. P., Snow T., Hanner M. S., Flynn G. J., Gezo J. C., Clemett S. J., Brownlee D. E., and Bowey J. E. 1999. An infrared spectral match between GEMS and interstellar grains. *Science* 285:1716–1718.

Brownlee D. E., Tomandl D. A., and Olszewski E. 1977. Interplanetary dust; A new source of extraterrestrial material for laboratory studies. Proceedings, 8th Lunar and Planetary Science Conference. pp. 9–160.

Brownlee D. E., Schramm L. S., Wheelock M. M., and Maurette M. 1989. Large mineral grains in interplanetary dust (abstract). 20th Lunar and Planetary Science Conference. pp. 121–122.

Brownlee D. E., Joswiak D. J., Bradley J. P., Schlutter D. J., and Pepin

R. O. 1998. Tiny bubbles: Direct observation of He in IDPS (abstract #1869). 29th Lunar and Planetary Science Conference. CD-ROM.

Brownlee D. E., Joswiak D. J., Schlutter D. J., Pepin R. O., Bradley J. P., and Love S. G. 1995. Identification of individual cometary IDPs by thermally stepped He release (abstract). 26th Lunar and Planetary Science Conference. pp. 183–184.

Ceplecha Z., Spalding R. E., Jacobs C., and Tagliaferri E. 1996. Luminous efficiencies of bolides. *Proceedings of SPIE* 2813:46–56.

Cliff G. and Lorimer G. W. 1975. The quantitative analysis of thin specimens. *Journal of Microscopy* 103:203–207.

Christoffersen R. and Buseck P. R. 1986. Mineralogy of interplanetary dust particles from the "olivine" infrared class. *Earth and Planetary Science Letters* 78:53–66.

Condit R. H., Hobbins R. R., and Birchenal C. E. 1974. Self-diffusion of iron and sulfur in ferrous sulfide. *Oxidation of Metals* 8:409–455.

Dai Z. R. and Bradley J. P. 2001. Iron-nickel sulfides in anhydrous interplanetary dust particles. *Geochimica et Cosmochimica Acta* 65:3601–3612.

Dermott S. F., Grogan K., Gustafson B. Å. S., Jayaraman S., Kortenkamp S. J., and Xu Y. L. 1996. Sources of interplanetary dust. In *Physics, chemistry, and dynamics of interplanetary dust,* edited by Gustafson B. Å. S. and Hanner M. S. San Francisco: Anstronomical Society of the Pacific. *Astronomical Society of the Pacific Conference Series* 104:143–153.

Flynn G. J. 1994. Changes to the composition and mineralogy of interplanetary dust particles by terrestrial encounters. In *Analysis of interplanetary dust,* edited by Zolensky M. E., Wilson T. L., Rietmeijer F. J. M., and Flynn G. J. New York: American Institute of Physics Press. *American Institute of Physics Conference Proceedings* 310:127–143.

Flynn G. J. 1995. Thermal gradients in interplanetary dust particles: The effect of an endothermic phase transition (abstract). 26th Lunar and Planetary Science Conference. pp. 405–406.

Flynn G. J. 1996. Sources of 10 micron interplanetary dust: The contribution from the Kuiper belt. In *Physics, chemistry, and dynamics of interplanetary dust,* edited by Gustafson B. Å. S. and Hanner M. S. San Francisco: Anstronomical Society of the Pacific. *Astronomical Society of the Pacific Conference Series* 104:171–175.

Fraundorf P. 1981. Interplanetary dust in the transmission electron microscope: Diverse materials from the early solar system. *Geochimica et Cosmochimica Acta* 45:915–943.

Germani M. S., Bradley J. P., and Brownlee D. E. 1990. Automated thin-film analyses of hydrated interplanetary dust particles in the analytical electron microscope. *Earth and Planetary Science Letters* 101:162–179.

Graham J. and McKenzie C. D. 1987. Oxygen in pyrrhotite: 2. Determination of oxygen in natural pyrrhotites. *American Mineralogist* 72:605–609.

Halliday I., Griffin A. A., and Blackwell A. T. 1996. Detailed data for 259 fireballs from the Canadian camera network and inferences concerning the influx of large meteoroids. *Meteoritics & Planetary Science* 31:185–217.

Hong Y. and Fegley B., Jr. 1997. The kinetics and mechanism of pyrite thermal decomposition. *Berichte der Bunsen-Gesellschaft für Physikalische Chemie* 101:1870–1881.

Huebner J. S. and Turnock A. C. 1980. The melting relations at 1 bar of pyroxenes composed largely of Ca-, Mg-, and Fe-bearing components. *American Mineralogist* 65:225–271.

Jessberger E. K., Christoforidis A., and Kissel J. 1988. Aspects of major element composition of Halley's dust. *Nature* 332:691–695.

Joswiak D. J., Brownlee D. E., Pepin R. O., and Schlutter D. J. 2000. Characteristics of asteroidal and cometary IDPs obtained from stratospheric collectors: Summary of measured He release temperatures, velocities, and descriptive mineralogy (abstract #1500). 31st Lunar and Planetary Science Conference. CD-ROM.

Keller L. P., Messenger S., and Bradley J. P. 2000. Analysis of a deuterium-rich interplanetary dust particle and implications for presolar materials in IDPs. *Journal of Geophysical Research—Space Physics* 105:10397–10402.

Keller L. P., Hony S., Bradley J. P., Molster F. J., Waters L. B. F. M., Bouwman J., de Koter A., Brownlee D. E., Flynn G. J., Henning T., and Mutschke H. 2002. Identification of iron sulphide grains in protoplanetary disks. *Nature* 417:148–150.

Klöck W. and Stadermann F. J. 1994. Mineralogical and chemical relationships of interplanetary dust particles, micrometeorites, and meteorites. In *Analysis of interplanetary dust,* edited by Zolensky M. E., Wilson T. L., Rietmeijer F. J. M., and Flynn G. J. New York: American Institute of Physics Press. *American Institute of Physics Conference Proceedings* 310:51–87.

Kübler L. 1982. A continuous phase gradient in a "monocrystalline" pyrrhotite. *Physics and Chemistry of Minerals* 8:8–13.

Kullerud G., Yund R. A., and Moh G. H. 1969. Phase relations in the Cu-Fe-S, Cu-Ni-S, and Fe-Ni-S systems. *Economic Geology* Monograph 4:323–343.

Lauretta D. S., Kremser D. T., and Fegley B., Jr. 1996. The rate of iron sulfide formation in the solar nebula. *Icarus* 122:288–315.

Lawler M. E. and Brownlee D. E. 1992. CHON as a component of dust from comet Halley. *Nature* 359:810–812.

Likhachev A. P. and Brauer Yu. A. 1969. The thermal stability of pentlandite. *Doklady Earth Sciences* 186:154–156.

Llorca J. and Casanova I. 2000. Reaction between H_2, CO, and H_2S over Fe, Ni metal in the solar nebula: Experimental evidence for the formation of sulfur-bearing organic molecules and sulfides. *Meteoritics & Planetary Science* 35:841–848.

Love S. G. and Brownlee D. E. 1991. Heating and thermal transformation of micrometeoroids entering the Earth's atmosphere. *Icarus* 89:26–43.

Love S. G. and Brownlee D. E. 1994. Peak atmospheric entry temperatures of micrometeorites *Meteoritics & Planetary Science* 29:69–70.

Mackinnon I. D. R. and Kaser S. A. 1987. Microbeam analysis of clays at low temperature. In *Microbeam analysis 1987,* edited by Geiss R. H. San Francisco: San Francisco Press. pp. 332–334.

Mackinnon I. D. R. and Rietmeijer F. J. M. 1987. Mineralogy of chondritic interplanetary dust particles. *Reviews of Geophysics* 25:1527–1553.

Mackinnon I. D. R., McKay D. S., Nace G., and Isaacs A. M. 1982. Classification of the Johnson Space Center stratospheric dust collection. Proceedings, 13th Lunar and Planetary Science Conference. *Journal of Geophysical Research* 87:A413–A421.

McKeegan K. D. 1987. Oxygen isotopes in refractory stratospheric dust particles: Proof of extraterrestrial origin. *Science* 237:1468–1471.

Meibom A., Petaev M. I., Krot A. N., Wood J., and Keil. K. 1999. Primitive FeNi metal grains in CH carbonaceous chondrites formed by condensation from a gas of solar composition. *Journal of Geophysical Research* 104:22053–22059.

Messenger S. 2000. Identification of molecular-cloud material in interplanetary dust particles. *Nature* 404:968–971.

Messenger S., Keller L. P., Stadermann F. J., Walker R. M., and Zinner E. 2003. Samples of stars beyond the solar system: Silicate grains in interplanetary dust. *Science* 300:105–108.

Murray I. S., Beech M., Taylor M. J., and Hawkes R. L. 2000. Comparison of 1998 and 1999 Leonid light curve morphology and meteoroid structure. *Earth, Moon, Planets* 82–83:351–367.

Nier A. O. and Schlutter D. J. 1993. The thermal history of interplanetary dust particles collected in the Earth's stratosphere. *Meteoritics* 28:675–681.

Nuth J. A., III, Hallenbeck S. L., and Rietmeijer F. J. M. 2000. Laboratory studies of silicate smokes: Analog studies of circumstellar materials. *Journal of Geophysical Research* 105: 10387–10396.

Nuth J. A., III, Rietmeijer F. J. M. and Hill H. G. M. 2002. Condensation processes in astrophysical environments: The composition and structure of cometary grains. *Meteoritics & Planetary Science* 37:1579–1590.

Ohsumi K. and Zolensky M. E. 1998, Synchrotron XRD studies on interplanetary dust particles L2005AE6 and L2005AG17 (abstract). 17th General Meeting of the International Mineralogical Association.

Posfai M., Sharp T. G., and Kontny A. 2000. Pyrrhotite varieties from the 9.1 km deep borehole of the KTB project. *American Mineralogist* 85:1406–1415.

Rietmeijer F. J. M. 1985. A model for diagenesis in proto-planetary bodies. *Nature* 313:293–294.

Rietmeijer F. J. M. 1988. Sulfides and oxides in comets. *The Astrophysical Journal* 331:L137–L138.

Rietmeijer F. J. M. 1991. Aqueous alteration in five chondritic porous interplanetary dust particles. *Earth and Planetary Science Letters* 102:148–157.

Rietmeijer F. J. M. 1992. Endothermic reactions constrain dynamic pyrometamorphic temperatures in two iron-rich interplanetary dust particles (abstract). 23rd Lunar and Planetary Science Conference. pp. 1151–1152.

Rietmeijer F. J. M. 1996a. Cellular precipitates of iron-oxide in olivine in a stratospheric interplanetary dust particle. *Mineralogical Magazine* 60:877–885.

Rietmeijer F. J. M. 1996b. The ultrafine mineralogy of a molten interplanetary dust particle as an example of the quench regime of atmospheric entry heating. *Meteoritics & Planetary Science* 31:237–242.

Rietmeijer F. J. M. 1996c. CM-like interplanetary dust particles in the lower stratosphere during 1989 October and 1991 June/July. *Meteoritics & Planetary Science* 31:278–288.

Rietmeijer F. J. M. 1998. Interplanetary dust particles. In *Planetary materials,* edited by Papike J. J. Washington D.C.: Mineralogical Society of America. pp. 2-1–2-95.

Rietmeijer F. J. M. 1999. Metastable non-stoichiometric diopside and Mg-wollastonite: An occurrence in an interplanetary dust particle. *American Mineralogist* 84:1883–1894.

Rietmeijer F. J. M. 2000. Interrelationships among meteoric metals, meteors, interplanetary dust, micrometeorites, and meteorites. *Meteoritics & Planetary Science* 35:1025–1041.

Rietmeijer F. J. M. 2002a. The earliest chemical dust evolution in the solar nebula. *Chemie Erde* 62:1–45.

Rietmeijer F. J. M. 2002b. Shower meteoroids: Constraints from interplanetary dust particles and Leonid meteors. *Earth, Moon, and Planets* 88:35–58.

Rietmeijer F. J. M. and Karner J. M. 1999. Metastable eutectics in the Al_2O_3-SiO_2 system explored by vapor phase condensation. *Journal of Chemical Physics* 110: 4554–4558.

Rietmeijer F. J. M. and Mackinnon I. D. R. 1985a. Layer silicates in a chondritic porous interplanetary dust particle. Proceedings, 16th Lunar and Planetary Science Conference. *Journal of Geophysical Research* 90:D149–D155.

Rietmeijer F. J. M. and Mackinnon I. D. R. 1985b. A multi-stage history for carbonaceous material in extraterrestrial chondritic porous aggregate W7029*A and a new cosmothermometer (abstract). 16th Lunar and Planetary Science Conference. pp. 700–701.

Rietmeijer F. J. M., Mukhin L. M., Fomenkova M. N., and Evlanov E. N. 1989. Layer silicate chemistry in P/comet Halley from PUMA-2 data (abstract). 20th Lunar and Planetary Science Conference. pp. 904–905.

Rietmeijer F. J. M., Nuth J. A., III, and Karner J. M. 1999. Metastable eutectic condensation in a Mg-Fe-SiO-H_2-O_2 vapor: Analogs to circumstellar dust. *The Astrophysical Journal* 527:395–404.

Rietmeijer F. J. M., Nuth J. A., III, Jablonska M., and Karner J. M. 2000. Metastable eutectic equilibrium in natural environments: Recent developments and research opportunities. *Trends in Geochemistry* 1:29–51.

Rietmeijer F. J. M., Hallenbeck S. L., Nuth J. A., III, and Karner J. M. 2002. Amorphous magnesiosilicate smokes annealed in vacuum: The evolution of magnesium silicates in circumstellar and cometary dust. *Icarus* 156:269–286.

Rietmeijer F. J. M., Nuth J. A., III, and Nelson R. N. 2004. Laboratory hydration of condensed magnesiosilica smokes with implications for hydrated silicates in IDPs and comets. *Meteoritics & Planetary Science* 39:723–746.

Rost D., Stephan T., and Jessberger E. K. 1999. Surface analysis of stratospheric dust particles. *Meteoritics & Planetary Science* 34: 637–646.

Sandford S. A. and Walker R. M. 1985. Laboratory infrared transmission spectra of individual interplanetary dust particles from 2.5 to 25 microns. *The Astrophysical Journal* 291:838–851.

Schramm L. S. and Brownlee D. E. 1990. Iron-nickel sulfides in interplanetary dust (abstract). 21st Lunar and Planetary Science Conference. pp. 1093–1094.

Schramm L. S., Brownlee D. E., and Wheelock M. M. 1989. Major element composition of stratospheric micrometeorites. *Meteoritics* 24:99–112.

Steele I. M. 1990. Minor elements in forsterites of Orgueil (Cl), Alais (Cl), and two interplanetary dust particles compared to C2-C3-UOC forsterites. *Meteoritics* 25:301–307.

Thomas K. L., Keller L. P., Klöck W., and McKay D. S. 1991. Mineralogical and chemical constraints on parent bodies for hydrated interplanetary dust particles (abstract). 22nd Lunar and Planetary Science Conference. pp. 1395–1396.

Thomas K. L., Blanford G. E., Clemett S. J., Flynn G. J., Keller L. P., Klöck W., Maechling C. R., McKay D. S., Messenger S., Nier A. O., Schlutter D. J., Sutton S. R., Warren J. L., and Zare R. N. 1995. An asteroidal breccia: The anatomy of a cluster IDP. *Geochimica et Cosmochimica Acta* 59:2797–2815.

Tomeoka K. and Buseck P. R. 1984. Transmission electron microscopy of the "LOW-CA" hydrated interplanetary dust particle. *Earth and Planetary Science Letters* 69:243–254.

Warren J. L. and Zolensky M. E. 1994. Collection and curation of interplanetary dust particles recovered from the stratosphere. In *Analysis of interplanetary dust,* edited by Zolensky M. E., Wilson T. L., Rietmeijer F. J. M., and Flynn G. J. New York: American Institute of Physics Press. *American Institute of Physics Conference Proceedings* 310:105–114.

Zolensky M. E. 1987. Refractory interplanetary dust particles. *Science* 237:1466–1468.

Zolensky M. and Barrett R. 1994. Compositional variations of olivines and pyroxenes in chondritic interplanetary dust particles. *Meteoritics* 29:616–620.

Zolensky M. E. and Thomas K. L. 1995. Iron- and iron-nickel sulfides in chondritic interplanetary dust particles. *Geochimica et Cosmochimica Acta* 59:4707–4712.

Zolensky M., Nakamura K., Weisberg M. K., Prinz M., Nakamura T., Ohsumi K., Saitow A., Mukai M., and Gounelle M. 2003. A primitive dark inclusion with radiation-damaged silicates in the Ningqiang carbonaceous chondrite. *Meteoritics & Planetary Science* 38:305–322.